

A systematic approach to riser VIV response reconstruction

H. Mukundan^{*}, F.S. Hover, M.S. Triantafyllou

Center for Ocean Engineering, Massachusetts Institute of Technology, 77 Massachusetts Avenue, Cambridge, MA, USA

Received 20 September 2008; accepted 24 March 2010

Abstract

Vortex-induced vibration (VIV) of long flexible cylindrical structures (e.g. risers, pipelines, tendons, mooring lines) enduring ocean currents is ubiquitous in the offshore industry. Though significant effort has gone into understanding this complicated fluid–structure interaction problem, major challenges remain in modeling and predicting the response of such structures (for example a riser). The work presented in this paper provides a systematic approach to estimate and analyze the vortex-induced motions of a marine riser. A systematic framework is developed, which allows reconstruction of the riser motion from a limited number of sensors placed along its length. A full reconstruction criterion is developed, which classifies when the measurements from the sensors contain all information pertinent to riser VIV response, and when they do not, in which case additional, analytical methods must be employed. Reconstruction methods for both scenarios are developed and applied to experimental data. Finally, a systematic study on the error during the reconstruction is also undertaken. The methods developed in this paper can be applied to: improve understanding of the vortex shedding mechanisms, including the presence of traveling waves and higher-harmonic forces; develop tools for in-situ estimation of fatigue damage on marine risers; and estimate the vortex-induced forces on marine risers.

© 2010 Elsevier Ltd. All rights reserved.

Keywords: Vortex-induced vibration; Marine risers; Response reconstruction; Full reconstruction criterion; Peak response modes; Peak response frequencies

1. Introduction

Vortex-induced vibration (VIV) of ocean structures is a major factor affecting all stages of development of offshore structures (conceptualization, design, analysis, construction and monitoring) and governs the arrangement of risers and tendons, details during fabrication, method of installation and instrumentation, and operation. Advances to deeper waters in search for petroleum resources have resulted in multi-billion dollar offshore projects off the Gulf of Mexico, for example: Cheyenne, Independence Hub, Perdido, Atlantis, Nakika, Thunder Horse to name a few. In such water depths, long flexible cylinders are increasingly required (umbilicals, tendons, mooring lines, risers, conductor tubes, pipeline spans), and prediction of their VIV response has become increasingly important.

The present schemes for predicting riser VIV are based on a number of hypotheses and experimental observations. These experimental observations are conducted primarily on stationary rigid cylinders and flexibly mounted rigid

^{*}Corresponding author. Tel.: +1 857928 2186.

E-mail address: harishm@alum.mit.edu (H. Mukundan).

cylinders. As such, several characteristics of flexible cylinder VIV remains not well understood. Understanding the complicated fluid–structure interaction problem of riser VIV requires careful observation of riser motions. Knowing the riser VIV motions allows us to estimate the vortex-induced forces, and predict the vortex-induced dynamic stresses and stress hot-spots on the riser, which in-turn allows us to predict the fatigue damage on the riser. For this purpose, ideally we need to obtain the measurements at all points along the length of the riser and study the riser VIV motions. However, in reality the riser motions are measured using sensors placed at select locations along its span. In such a scenario, there is a need to intelligently complete the information on the riser vortex-induced motions by using the data measured from the sensors.

1.1. Problem setting

Consider a flexible riser of length L taut along the z -axis as shown in Fig. 1. Assume we have N_s sensors placed along the riser at locations $z_1, z_2, \dots, z_s, \dots, z_{N_s}$. These sensors may measure displacements $y(z_s, t_j)$, accelerations $a(z_s, t_j)$ or bending induced axial strains $\varepsilon_{zz}(z_s, t_j)$.

Before we develop the solution process, it is important to consider the characteristics of the sensor measurements and the riser VIV motions. The measurements from these sensors have the following characteristics.

- (i) *High temporal sampling rate.* Each of the sensors measures the signal with high sampling rate in time. These samples are usually uniform and these measurements are obtained for a sufficiently long period of time.
- (ii) *Limited number of sensors.* Measurements of VIV responses are typically limited to a relatively small number of sensors located along the riser length. A large number of sensors in field data is very expensive due to installation, instrumentation and upkeep costs, especially since these sensors must be light and of small volume so they do not affect the properties of the riser; also several sensors may fail during long testing periods. In addition, the sensors are often unevenly placed or become uneven due to the failure of some of them. Due to the above reasons, the scenario of having data from a large number of sensors placed along a riser is typically possible only in a controlled setup like an experiment [e.g., Lie and Kaasen (2006); Kaasen et al. (1997)].
- (iii) *Indirect measurement of displacement.* Presently, direct measurement of riser displacements are not feasible. Vortex-induced motions along a riser are typically measured as accelerations (using accelerometers) or strains (using strain gauges) at select locations along the riser. A typical experimental measurement would consist of data from both accelerometers and strain gauges.

In addition, the riser motions due VIV has the following characteristics.

- (a) *Narrow banded in time:* Several experiments conducted in the laboratory and field suggests that the riser displacements due to vortex shedding occurs around a preferred frequency band around the local Strouhal frequency.
- (b) *Narrow banded in space:* In addition, the temporal frequency ω and spatial frequency (wave number) k are related through the dispersion relationship [refer to Graff (1991)]. Since the displacement spectra are band limited in ω , the displacement spectra are band limited in k although the spread of the band could be affected due to the variability in *effective added mass* in addition to any variation in stiffness along the riser.

Since the sampling in time is typically very dense, for the purpose of explaining the concept, we can consider t as a continuous variable. The discrete nature of the measured time signal will be appropriately taken care of during the implementation stage. We define *response reconstruction* as the process of using the data from these sensors ($y(z_s, t_j)$, $a(z_s, t_j)$, $\varepsilon_{zz}(z_s, t_j)$) and obtaining the displacements $y(z, t)$ at any arbitrary location z along the riser.

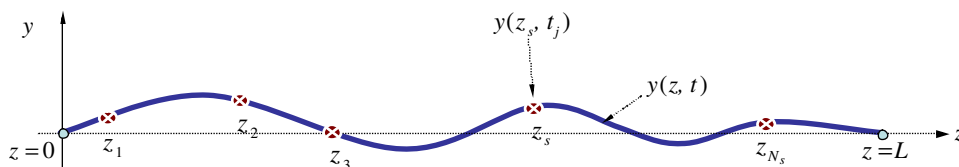


Fig. 1. Figure depicting a typical arrangement of sensors on a riser.

1.2. A review of related literature

Several researchers have considered the response reconstruction problem; the relevant references include Kaasen et al. (1997); Trim et al. (2005), and Lie and Kaasen (2006). These methods are based on linear structural dynamics techniques combined with the classical mode superposition principle, where the displacements are written as a linear combination of the classical riser free vibration modes weighted by the modal response factors. The classical free vibration modes are used as a complete basis to project the resulting vibration.

The present methodology differs with respect to prior publications in that the spatial responses at each frequency are allowed to be different from the classical free vibration modes. This results in economy of representation, since the response is caused by vortex shedding which may not be of uniform phase. As a result, traveling waves are possible as shown by Mukundan (2008)—the need to transfer energy in sheared current cases from a lockin region to a damping region makes this argument even stronger. Also, the large variability in the added mass along the riser may affect the patterns of response. In addition, the vortex-induced motion of a riser is a forced vibration rather than a free vibration, involving complicated fluid forces, possibly of a traveling wave type.

Using the riser response modes from semi-empirical prediction codes like VIVA [refer to Triantafyllou (2006)] and SHEAR7 [refer to Vandiver (2003)] may be inadequate due to the differences between the prediction and the actual response. Moreover, the complicated riser response features the presence of boundary layers (small layers adjacent to the ends of the riser wherein there is a sharp change of curvature due to the singular effects of bending stiffness; so named in analogy with boundary layers in fluid mechanics). This further complicates the reconstruction when we are faced with strain signals and derivatives of numerically evaluated response modes. What is needed is a consistent and systematic approach to the reconstruction problem which is independent of predicting the riser response modes and can use measured displacement derivatives (acceleration and curvature/strain).

The criterion for the applicability of reconstruction method [refer to Lie and Kaasen (2006), Vandiver and Marcollo (2003), Trim et al. (2005)] is posed from a matrix inversion point of view, based on the number of modes needed in the modal analysis and number of sensors available. This criterion is hence sensitive to the choice and applicability of the response modes. We develop a criterion for full reconstruction which is independent of the choice of the response modes.

At present, we are not aware of any publications which attempts to consider the case when we have so few sensors such that the full reconstruction criterion is not satisfied. There is a definite need to address this issue and use the data from these sensors and produce intelligent estimation of the reconstructed riser response.

1.3. Solution overview and paper outline

While considering the solution strategy, it is very useful to think in terms of the displaced shape of the riser at any given instance of time or a snapshot of the riser undergoing VIV. The problem then becomes one where we use the spatial samples (measured at the sensor locations) to recreate the displaced shape of the riser at any instance of time. As will be shown in Section 3 of the paper, two fundamentally different scenarios emerge based on the available number of sensors and the relative bandwidth of the observed VIV motions of the riser.

Scenario I: When complete information of the riser VIV motion is present in the data obtained from the N_s sensors. Such a scenario arises due to the narrow-banded nature of the riser VIV response. This scenario happens when we are performing an experiment using a sensor array, and the key idea is to understand the riser VIV response and predict the fatigue damage on the riser. Under this scenario, we will pose the reconstruction problem from the perspective of a Fourier decomposition of the displaced shape of the riser.

Scenario II: The number of sensors are so few that the data obtained from these sensors alone is not enough to completely describe the riser VIV motions. This typically happens in the field where due to the expensive installation, instrumentation and upkeep costs, only a few sensors are mounted on the riser. The idea here is often to use the reconstructed riser motions to predict the remaining fatigue life on the riser. In such a scenario, the riser motions are completed using our prior understanding of riser VIV.

This paper is structured as follows. In Section 2 we will focus on the first scenario, where the number of sensors are high enough to completely describe the riser motions. For this, in Section 3, we will obtain the criterion for full reconstruction to determine when we do have enough number of sensors or when we do not have enough sensors. The reconstruction method for the scenario when few sensors are available is developed in Section 4. The above methods

will be applied to datasets from the Norwegian deepwater programme (NDP) experiments and the results are illustrated in Section 6. We will then attempt to quantify the error during reconstruction in Section 7.

2. Response reconstruction when large number of sensors are available

In a scenario when data from a large number of sensors are available so that the full reconstruction criterion (refer to Section 3) is met, the problem of reconstructing the riser VIV response is posed as a *spatial Fourier decomposition*. The displaced shape of the riser at any instance of time is expanded as a spatial Fourier series in terms of both the sine and cosine terms as

$$y(z, t) = a_0(t) + \sum_{n=1}^{\infty} \left[a_n(t) \cos\left(\frac{n\pi}{L} z\right) + b_n(t) \sin\left(\frac{n\pi}{L} z\right) \right]. \quad (1)$$

However, due to the narrow-banded nature of the riser motions, we can write the displaced shape of the riser in terms of a finite number of sine and cosine terms as

$$y(z, t) \approx a_0(t) + \sum_{n=1}^{N_m} \left[a_n(t) \cos\left(\frac{n\pi}{L} z\right) + b_n(t) \sin\left(\frac{n\pi}{L} z\right) \right] = \sum_{n=1}^{2N_m+1} w_n(t) \phi_n(z), \quad (2)$$

where $\phi_n(z)$ is a proxy for the sine and cosine terms and $w_n(t)$ the proxy corresponding to the Fourier coefficients $a_n(t)$ and $b_n(t)$. It is to be noted that both the sine and the cosine terms are important during reconstruction and this will be discussed in detail at a later part of this paper.

Presently, in real-world applications, we do not have the luxury of measuring the displacements directly. More often than not, we have a combination of sensors measuring accelerations, strains or displacements. In such a case where we need to use information from both strain gauges and accelerometers, we formulate the problem in a slightly different way. As the first step we relate the bending strains $\varepsilon_{zz}(z, t)$ measured on the surface of the riser to the local curvature $\kappa(z, t)$ as $\kappa(z, t) = (2/D)\varepsilon_{zz}(z, t)$, where D is the diameter of the riser. Thus we are presented with curvature $\kappa(z_{sk}, t)$, acceleration $a(z_{sa}, t)$ and displacement $y(z_{sy}, t)$ measurements at select locations along the riser. Using Eq. (2) we can write the curvature and acceleration of the riser under bending as

$$\kappa(z, t) \approx y_{zz}(z, t) = \sum_{n=1}^{2N_m+1} w_n(t) \phi_{n_{zz}}(z) \quad \text{and} \quad a(z, t) = y_{tt}(z, t) = \sum_{n=1}^{2N_m+1} w_{n_t}(t) \phi_n(z). \quad (3)$$

The purpose is to find the Fourier coefficients $w_n(t)$ at every instance of time. Posing Eqs. (2)–(3) in a matrix form to solve for $w_n(t)$ presents an additional difficulty due to the presence of $w_{n_t}(t)$ in addition to unknown $w_n(t)$. To mitigate this issue, the problem is posed in the frequency domain. This part of our approach closely follows the idea proposed to combine strain and acceleration measurements by Lie and Kaasen (2006). Since each of the sensors measures the signals at high time sampling rates over several cycles of the data we can take their Fourier transforms in time. If we denote the Fourier transforms: $\mathcal{F}\{w_n(t)\}$ by $\hat{w}_n(\omega)$, $\mathcal{F}\{y(z, t)\}$ by $\hat{y}(z, \omega)$, $\mathcal{F}\{a(z, t)\}$ by $\hat{a}(z, \omega)$, and $\mathcal{F}\{\kappa(z, t)\}$ by $\hat{\kappa}(z, \omega)$, we can write

$$\hat{y}(z, \omega) = \sum_{n=1}^{2N_m+1} \hat{w}_n(\omega) \phi_n(z), \quad \hat{a}(z, \omega) = -\omega^2 \sum_{n=1}^{2N_m+1} \hat{w}_n(\omega) \phi_n(z) \quad \text{and} \quad \hat{\kappa}(z, \omega) = \sum_{n=1}^{2N_m+1} \hat{w}_n(\omega) \phi_{n_{zz}}(z). \quad (4)$$

Posing the problem in frequency domain allows us to explicitly solve for $\hat{w}_n(\omega)$ by putting together Eqs. (4) in a matrix form. Also accounting for the discrete nature of the frequencies $\omega_1, \omega_2, \dots, \omega_l, \dots, \omega_A$, we obtain the corresponding matrix equation as

$$\underbrace{\begin{bmatrix} \phi_1(z_1) & \phi_2(z_1) & \dots & \phi_N(z_1) \\ \phi_1(z_2) & \phi_2(z_2) & \dots & \phi_N(z_2) \\ \phi_1(z_3) & \phi_2(z_3) & \dots & \phi_N(z_3) \\ \vdots & \vdots & \ddots & \vdots \\ \phi_1(z_{M_y}) & \phi_2(z_{M_y}) & \dots & \phi_N(z_{M_y}) \\ \phi_1(z_1) & \phi_2(z_1) & \dots & \phi_N(z_1) \\ \phi_1(z_2) & \phi_2(z_2) & \dots & \phi_N(z_2) \\ \phi_1(z_3) & \phi_2(z_3) & \dots & \phi_N(z_3) \\ \vdots & \vdots & \ddots & \vdots \\ \phi_1(z_{M_a}) & \phi_2(z_{M_a}) & \dots & \phi_N(z_{M_a}) \\ \phi_1''(z_1) & \phi_2''(z_1) & \dots & \phi_N''(z_1) \\ \phi_1''(z_2) & \phi_2''(z_2) & \dots & \phi_N''(z_2) \\ \phi_1''(z_3) & \phi_2''(z_3) & \dots & \phi_N''(z_3) \\ \vdots & \vdots & \ddots & \vdots \\ \phi_1''(z_{M_k}) & \phi_2''(z_{M_k}) & \dots & \phi_N''(z_{M_k}) \end{bmatrix}}_{\Phi} \underbrace{\begin{bmatrix} \hat{w}_1(\omega_1) & \hat{w}_1(\omega_2) & \dots & \hat{w}_2(\omega_A) \\ \hat{w}_2(\omega_1) & \hat{w}_2(\omega_2) & \dots & \hat{w}_2(\omega_A) \\ \hat{w}_3(\omega_1) & \hat{w}_3(\omega_2) & \dots & \hat{w}_3(\omega_A) \\ \vdots & \vdots & \ddots & \vdots \\ \hat{w}_N(\omega_1) & \hat{w}_N(\omega_2) & \dots & \hat{w}_N(\omega_A) \end{bmatrix}}_{\hat{\mathbf{w}}} = \underbrace{\begin{bmatrix} \hat{y}(z_1, \omega_1) & \hat{y}(z_1, \omega_2) & \dots & \hat{y}(z_1, \omega_A) \\ \hat{y}(z_2, \omega_1) & \hat{y}(z_2, \omega_2) & \dots & \hat{y}(z_2, \omega_A) \\ \hat{y}(z_3, \omega_1) & \hat{y}(z_3, \omega_2) & \dots & \hat{y}(z_3, \omega_A) \\ \vdots & \vdots & \ddots & \vdots \\ \hat{y}(z_{M_y}, \omega_1) & \hat{y}(z_{M_y}, \omega_2) & \dots & \hat{y}(z_{M_y}, \omega_A) \\ \frac{-\hat{a}(z_1, \omega_1)}{\omega_1^2} & \frac{-\hat{a}(z_1, \omega_2)}{\omega_2^2} & \dots & \frac{-\hat{a}(z_1, \omega_A)}{\omega_A^2} \\ \frac{-\hat{a}(z_2, \omega_1)}{\omega_1^2} & \frac{-\hat{a}(z_2, \omega_2)}{\omega_2^2} & \dots & \frac{-\hat{a}(z_2, \omega_A)}{\omega_A^2} \\ \frac{-\hat{a}(z_3, \omega_1)}{\omega_1^2} & \frac{-\hat{a}(z_3, \omega_2)}{\omega_2^2} & \dots & \frac{-\hat{a}(z_3, \omega_A)}{\omega_A^2} \\ \vdots & \vdots & \ddots & \vdots \\ \frac{-\hat{a}(z_{M_a}, \omega_1)}{\omega_1^2} & \frac{-\hat{a}(z_{M_a}, \omega_2)}{\omega_2^2} & \dots & \frac{-\hat{a}(z_{M_a}, \omega_A)}{\omega_A^2} \\ \hat{\kappa}(z_1, \omega_1) & \hat{\kappa}(z_1, \omega_2) & \dots & \hat{\kappa}(z_1, \omega_A) \\ \hat{\kappa}(z_2, \omega_1) & \hat{\kappa}(z_2, \omega_2) & \dots & \hat{\kappa}(z_2, \omega_A) \\ \hat{\kappa}(z_3, \omega_1) & \hat{\kappa}(z_3, \omega_2) & \dots & \hat{\kappa}(z_3, \omega_A) \\ \vdots & \vdots & \ddots & \vdots \\ \hat{\kappa}(z_{M_k}, \omega_1) & \hat{\kappa}(z_{M_k}, \omega_2) & \dots & \hat{\kappa}(z_{M_k}, \omega_A) \end{bmatrix}}_{\hat{\mathbf{Y}}}, \quad (5)$$

where $N = 2N_m + 1$. The above Eq. (5) in the frequency domain can be written in a compact form as $\Phi \hat{\mathbf{w}} = \hat{\mathbf{Y}}$, where Φ is the matrix containing the sine and cosine terms and their spatial derivatives evaluated at the sensor locations, and $\hat{\mathbf{Y}}$ is independent of the temporal frequency ω ; $\hat{\mathbf{Y}}$ is the Fourier transform of the measured experimental data (data matrix); $\hat{\mathbf{w}}$ is the matrix containing the unknown Fourier coefficients of the sine and cosine terms in the frequency domain. The solution for each ω can be obtained by taking a pseudo-inverse Φ^+ of Φ as $\hat{\mathbf{w}} = \Phi^+ \hat{\mathbf{Y}}$. By pseudo-inverse, we mean the process of solving an overconstrained system of equations in a least-square sense [refer to Morgan and Rao (2006)].

After solving for the Fourier coefficient matrix in the frequency domain to obtain $\hat{\mathbf{w}}$, one can easily obtain the Fourier coefficient matrix in the time domain \mathbf{w} by a simple inverse Fourier transform $\mathcal{IF}\{\}$. The displacements can then be reconstructed using Eq. (2). The overall solution methodology is described as a flowchart in Fig. 2.

It should be noted that for a general scenario involving data from both accelerometers and strain gauges, the accelerations (displacements) and curvatures may have completely different magnitudes depending primarily on the length of the riser. The result of such a scenario is an ill-conditioned system of equations. To rectify this situation, we need to scale either the equation corresponding to the acceleration measurements or the curvature measurements to bring them to similar order of magnitudes. This issue is mentioned in detail in Section 7.3.

2.1. A discussion on response reconstruction method using data from large number of sensors

During the actual implementation we need to obtain the pseudo-inverse Φ^+ only once, resulting in increased speed of the reconstruction algorithm. In addition, we do not need to consider all frequencies while solving for $\hat{\mathbf{w}}$. If the signals are band limited in the temporal frequency, then the signals with only the nonzero Fourier coefficients need to be evaluated.

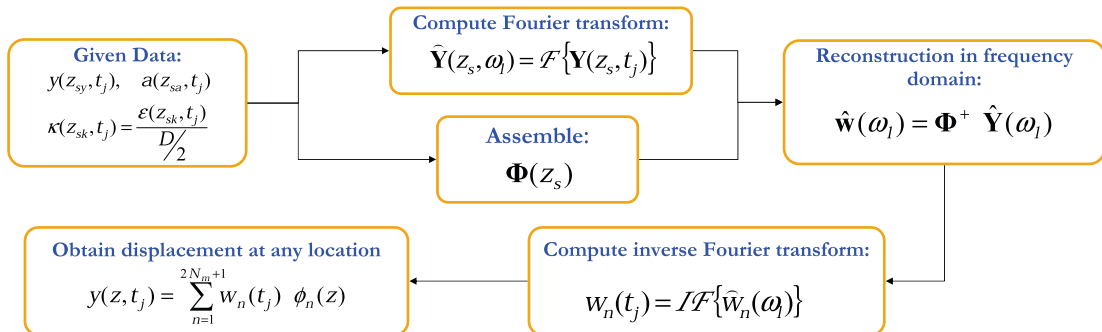


Fig. 2. Flowchart of the algorithm for reconstructing riser VIV displacements using data from large number of sensors (for scenario I).

Since the matrix Φ has a size $N_s \times (2N_m+1)$, obtaining the pseudo-inverse requires $N_s \geq (2N_m + 1)$. In practice, the error grows as the number of sensors comes close to this reconstruction criterion. As a result we have to require that N_m to be slightly lower than the critical value of $N_s/2$. Section 3 describes the full reconstruction criterion in much greater detail, while Section 7 describes an in depth study on the reconstruction error.

A few lower order spatial harmonics have to be removed while assembling the Φ matrix because of their extreme sensitivity to noise which is present in the real data. While preparing the data matrix \hat{Y} and the Φ matrix, the boundary conditions have to be enforced as extra constraints on the problem and in fact they are equivalent to additional sensors placed at the riser ends.

Need for both sine and cosine terms. Prior reconstruction methods [refer to Lie and Kaasen (2006)] have utilized the expansion of the riser VIV motions using sinusoidal modes which are the eigenmodes for a beam with homogeneous boundary conditions. The expansion using sinusoidal modes may seem similar to a Fourier expansion using only sine terms but is fundamentally different. The method we propose using spatial Fourier series require the cosine terms in addition to the sine terms.

One justification for using cosine terms is that the available datasets consists of both acceleration and curvature measurements. These displacement derivatives and their Fourier transforms taken in time could have boundary layer formation at the ends due to the complicated riser VIV motions (an example is traveling waves which is discussed in Section 6). Accurate representation of such a displaced shape requires enough flexibility for the interpolating curve and is not feasible with sine terms alone.

On the other hand, an initially curved beam with homogeneous boundary conditions has eigenmodes which are a combination of sine and cosine terms. During real world applications (pipelines) or in VIV model tests, the riser model may be oriented horizontally and may have an initial bend due to gravity and require cosine terms. The use of cosine terms are further justified by the results from various benchmarking tests we have performed and are mentioned in more detail in Section 6.1.1.

From a mathematical viewpoint, the reconstruction using sine and cosine terms assumes a periodic extension in the regime $z = [-L, L]$, where we have sensors placed only between $z = [0, L]$. It is also possible to assume an odd periodic extension in the regime $z = [-L, L]$ by placing hypothetical sensors in the region $z = [-L, 0]$. However, placing hypothetical sensors is an extra constraint which will result in major deviations observed in the reconstructed signal as shown in extensive benchmark tests given in Section 6.1.1. Using sine and cosine terms produces excellent accuracy otherwise impossible with only sine terms.

3. Full reconstruction criterion (spatial Nyquist–Shannon criterion)

The criterion for full reconstruction of a signal from its samples was first mentioned by Nyquist (1928), later by Shannon (1949) and is described in its present form in Oppenheim et al. (1997). The Nyquist–Shannon criterion (Nyquist’s criterion in short or sampling theorem) states that if we have a signal $y(z)$ with its Fourier transform $\hat{y}(k)$, such that $\hat{y}(k) = 0$, for $|k| > k_m$ (that is $y(z)$ is band-limited in spatial frequency k with a cutoff spatial frequency equal to k_m), then $y(z)$ is uniquely determined by its samples $y(n\Delta_z)$ if $k_s = 2\pi/\Delta_z > 2k_m$ where Δ_z is the spacing between the adjacent samples. In other words Nyquist’s criterion states that an exact reconstruction of a signal from its samples is possible if the signal is band-limited and the sampling frequency k_s is greater than two times the bandwidth of the signal k_m .

The reconstruction method with sine and cosine terms assumes a periodic extension of the signal with a period $z = [-L, L]$. Based on this, we can evaluate the Nyquist’s criterion by assuming N_s sensors placed (for simplicity we can assume uniformly placed) over a period $2L$ resulting in a spatial sampling frequency $k_s = 2\pi/2L/N_s = \pi N_s/L$. If we assume that the displaced shape of the pipeline or riser is such that the spatial frequency k is band-limited,¹ then the highest nonzero spatial harmonic present in the Fourier decomposition (N_m) is related to the spatial bandwidth as $k_m = \max[n\pi/L] = \pi N_m/L$. The Nyquist criterion then becomes $k_s > 2k_m$ or, $\pi N_s/L > 2(\pi N_m/L)$, or, $N_s > 2N_m$. However if we also include the constant term ($a_0(t)$), we obtain the criterion as

$$N_s \geq 2N_m + 1. \quad (6)$$

In other words, the number of sensors N_s should be greater than two times the number of spatial harmonics N_m present in the function $y(z)$ plus one. In practice, a more uniform distribution of sensors is found to yield better reconstruction

¹The spatial frequency (wave number) k is related to the temporal frequency ω through the dispersion relationship. Since the displacement spectra is band limited in ω , displacement spectra is band limited in k although the spread of the band could be affected due to the variability in effective added mass over the riser or pipeline.

accuracy than the presence of several sensors which are clustered. It is also interesting to note that the Nyquist criterion is a *sufficient condition* and is not a *necessary condition*. Note that this criterion matches the criterion we obtained based on obtaining the pseudo-inverse of Φ .

Instead of using both sine and cosine terms, if we assume that the riser displacements are restricted by assuming an odd periodic extension using only sine terms, the full reconstruction criterion is obtained as $N_s > N_m$. However, this assumption artificially introduces certain characteristics for riser VIV response which may or may not be valid. Violating the above full reconstruction criterion will lead to *spatial aliasing* which is observed as linearly dependent rows of the Φ matrix.

4. Response reconstruction when few number of sensors are available

Now, let us consider the scenario when measurements from very few sensors (in cross-flow (CF) direction) are available such that the full reconstruction criterion is not satisfied. Under such a scenario, the measurements from few sensors do not contain all information related to the riser VIV. Additional information is required to complete the riser motions, and this additional information comes from our prior knowledge of riser VIV (predictive capabilities). Since we require predictive capabilities, we need to assume that the following information on the riser and flow are available.

Riser properties: The riser has a diameter D , length L , mass per unit length m , structural damping constant b , bending stiffness EI , and effective tension T . All these quantities may vary along the span of the riser.

Flow properties: The riser encounters a steady current $U(z)$ along the in-line (IL) direction. The fluid around it has a density ρ_f , and we have a good estimate of the empirical lift force coefficient databases of the lift coefficient in phase with velocity C_{lv} and the added mass coefficient C_m .

Similar to the method described in Section 2, the method we propose is applicable to a combination of strain, acceleration and displacement measurements. However for the simplicity of discussion, let us assume that the sensors typically measure acceleration signals $a(z_s, t)$. We are required to use the data measured by the sensors $a(z_s, t)$, the flow and the riser properties and obtain the displacements $y(z, t)$ at any arbitrary location z along the riser.

For the scenario involving data from few sensors, we pose the problem from a structural dynamics perspective where we express the displaced shape of the riser at any instance of time as a linear combination of the *peak response modes* $Y_n(z)$ oscillating at the *peak response frequencies* ω_n as

$$y(z, t) = \text{Re} \left\{ \sum_{n=1}^{N_m} Y_n(z) e^{i\omega_n t} \right\}. \quad (7)$$

The above statement is identical to the statement of the modal decomposition presented in Lucor et al. (2006) and Mukundan (2008). It is important to note that these $Y_n(z)$ and ω_n are not the classical free vibration modes and the free vibration frequencies. These $Y_n(z)$ and ω_n are the result of an equilibria arising from a power balance where the fluid excites some part of the riser and the riser dissipates the energy at other parts. These N_m number of $Y_n(z)$ and ω_n are the additional information we intend to provide to the reconstruction problem, and can be obtained using a prediction program like VIVA (Triantafyllou, 2006). The prediction for $Y_n(z)$ and ω_n are based on solving a nonlinear eigenvalue problem (Triantafyllou, 1998) using the riser and flow properties with the help of empirical lift coefficient databases of C_{lv} and C_m . Since a physical process is never purely harmonic but narrow-banded, we can generalize the Eq. (7) to write the displaced shape of the riser as

$$y(z, t) = \text{Re} \left\{ \sum_{n=1}^{N_m} w_n(t) Y_n(z) \right\}, \quad (8)$$

where $w_n(t)$ are the narrow banded modal participation factors with spectra depicting one dominant peak frequency centered around ω_n (ideally $w_n(t) \equiv e^{i\omega_n t}$). Taking the Fourier transforms of both sides of Eq. (8), we obtain $\hat{y}(z, \omega) = \mathcal{F}\{y(z, t)\} = \sum_{n=1}^{N_m} \hat{w}_n(\omega) Y_n(z)$. The $\hat{w}_n(\omega)$ and $\hat{y}(z, \omega)$ are, respectively, the Fourier transforms of $w_n(t)$ and $y(z, t)$ taken along time. Corresponding to the measurements at the sensor locations z_s we can write

$$\hat{y}(z_s, \omega) = \sum_{n=1}^{N_m} \hat{w}_n(\omega) Y_n(z_s). \quad (9)$$

Thus, corresponding to the N_s sensors, we have N_s equations and N_m unknowns corresponding to each unknown \hat{w}_n . If $N_s > N_m$, then the above system of equations (written in a compact form as $\Psi \hat{\mathbf{w}} = \hat{\mathbf{Y}}$) can be solved by taking a pseudo-inverse of Ψ to obtain $\hat{w}_n(\omega)$ and then taking the inverse Fourier transform to obtain $w_n(t)$ and correspondingly the riser displacements $y(z, t)$ using Eq. (8). However, if N_s is few in comparison to N_m , writing the Eq. (9) in a matrix

form and solving it directly is not possible due to a condition where there are more unknowns than the number of equations. In such a scenario, we reformulate the Eqs. (9) in a different form by employing the band-separated nature of the riser VIV. We subdivide the spectrum of the original signal $\hat{y}(z_s, \omega)$ into N_m separate spectra $\hat{y}_{n\text{-filt}}(z_s, \omega)$ by bandpass filtering them around each of the peak response frequencies ω_n as depicted in an example given in Fig. 9. Typically this bandpass filtering is performed in the frequency domain, by choosing those frequency components of the spectrum which lies within the frequency bands. As a result, we have

$$\hat{y}_{n\text{-filt}}(z_s, \omega) = \hat{w}_n(\omega) Y_n(z_s). \tag{10}$$

Now for each n , we have N_s equations and only one unknown \hat{w}_n , resulting in scenarios where the number of equations are greater than the number of unknowns. Thus, for each n we solve for $\hat{w}_n(\omega)$, and take the inverse Fourier transform to obtain $w_n(t)$,

$$\hat{w}_n(\omega) = Y_n^+(z_s) \hat{y}_{n\text{-filt}}(z_s, \omega). \tag{11}$$

Instead of posing it as one matrix inversion problem with more unknowns than equations (under-determined system), we pose the problem as N_m inversion problems each of which is well behaved. Once we obtain $w_n(t)$, we can reconstruct the riser displacements using Eq. (8).

4.1. Overall algorithm

The algorithm is described in Fig. 3. A statistically stationary segment of the measured data $\mathbf{Y}(z_s, t)$ is first extracted using scalograms as mentioned in Mukundan (2008). Next, the Fourier transform of $\mathbf{Y}(z_s, t)$ is taken to obtain $\hat{\mathbf{Y}}(z_s, \omega)$. Corresponding to the input flow profile $U(z)$, a prediction program like VIVA is used to obtain the peak response modes $Y_n(z)$ and peak response frequencies ω_n . Next, the spectrum of each of the sensor data $\hat{\mathbf{Y}}(z_s, \omega)$ is subdivided into N_m separate spectra to obtain $\hat{\mathbf{Y}}_{n\text{-filt}}(z_s, \omega)$. These bands are each centered around the predictions of ω_n .

For each n , we need to evaluate the modal matrix $\Psi_n(z_s)$ and the data matrix $\hat{\mathbf{Y}}_{n\text{-filt}}(z_s, \omega)$. $\Psi_n(z_s)$ is identically equal to the peak response mode Y_n evaluated at the sensor locations z_s . The data matrix $\hat{\mathbf{Y}}_{n\text{-filt}}(z_s, \omega)$ is obtained as mentioned in the previous paragraph. A pseudo-inverse of $\Psi_n(z_s)$ is calculated for each n , and the corresponding $\hat{w}_n(\omega)$ is evaluated. An inverse Fourier transform of $\hat{w}_n(\omega)$ is taken to obtain $w_n(t)$. Once we obtain each $w_n(t)$, the riser displacements is reconstructed using Eq. (8).

4.2. A discussion on response reconstruction using data from few sensors

The method critically relies on accurate prediction of peak response frequencies and peak response modes of the riser. At present, our predictive capabilities are handicapped by the approximations involved while obtaining the empirical lift force coefficient databases (Mukundan et al., 2009). It is proposed that for effective use of this reconstruction

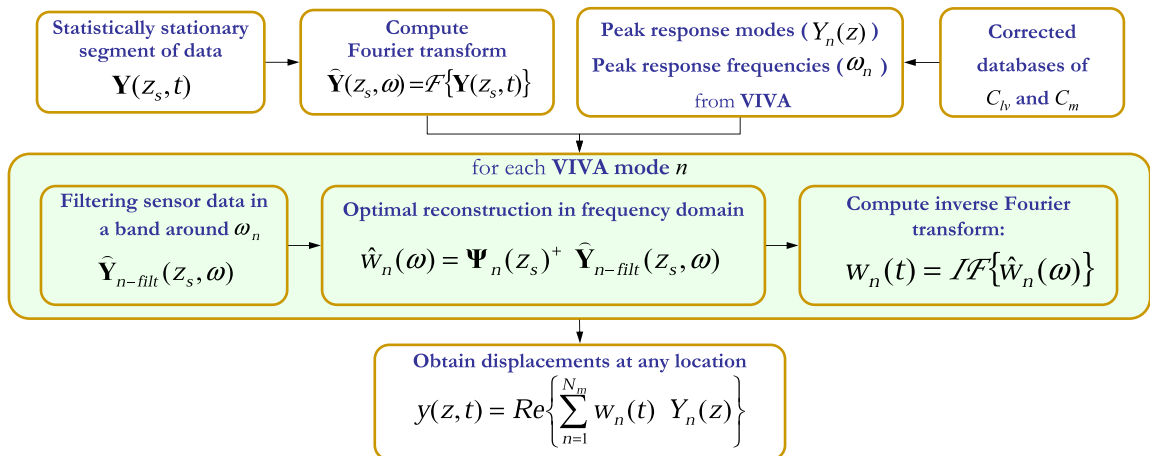


Fig. 3. Overview of the algorithm for reconstructing riser response using measurements from few sensors.

method, we are required to develop a method to correct the lift coefficient databases using data from the few available sensors. This lift coefficient database correction scheme for the purpose of response reconstruction is mentioned in Section 4.3.

The predictions of peak response modes require the flow velocity $U(z)$ which is required as an input to the prediction scheme (VIVA). It has been found that the estimates of the peak response modes are sensitive to the variation in flow velocity and hence affects the reconstruction itself.

The reconstruction method for the few sensor case differs from the reconstruction method for large number of sensors in many ways, as follows.

1. The present method is applicable even when the number of sensors are very few (as low as 2 or 3), unlike the case of reconstruction method for large number of sensors where the full reconstruction criterion needs to be satisfied.
2. The proposed method requires us to accurately obtain the flow profile $U(z)$, the fluid properties, and the riser properties. This is in contrast to the reconstruction method for large number of sensor case which is independent of the predictive capabilities and hence the riser properties or the flow properties.
3. To obtain the peak response modes and frequencies, we are required to assume a steady state response. However in reality this assumption is very difficult to be satisfied. However, we may be able to find stationary segments of the data over which this assumption is valid.
4. Instead of posing the reconstruction problem as one pseudo-inverse problem, we subdivide the problem into several well behaved problems by band pass filtering the signals around each peak response frequency ω_n .
5. We employ the use of peak response modes and frequencies obtained by solving a nonlinear eigenvalue problem. These modes and frequencies are very different from the classical free vibration modes used in the previously considered methods by Kaasen et al. (1997), Trim et al. (2005) and Lie and Kaasen (2006).
6. Since our predictive capabilities are limited to the riser CF motions, the reconstruction method in its present form is applicable to riser CF motions only. However, if a model for predicting the IL peak response modes and frequencies are evolved, then the reconstruction method is expected to work for IL motions also.
7. We have observed several datasets where a multi-moded response can clearly be considered as band-separated. However, we have also observed riser VIV response where such a separation is difficult, in which case the present theoretical explanations are limited and our reconstruction method may be used as a good first approximation.
8. Use of strain gauge measurements in addition to accelerometer measurements requires predictive capabilities for obtaining the curvature modes. These curvature modes can easily be obtained from displacement modes using a numerical scheme like the finite difference method.

4.3. Local lift coefficient database correction

The reconstruction method for few sensors depends on the accurate prediction of peak response modes and frequencies. For the case of real experimental data, the reconstruction problem can be subdivided into two subproblems: (i) the reconstruction problem given accurate prediction of peak response modes and peak response frequencies (mentioned in Section 4.1); and (ii) the problem of improving the predictions so that the predictions at the few sensor locations is consistent with the experimental data (theoretical estimates closely match the experimental observations). One source of error in the theoretical estimate is the uncertainty in the presently available lift coefficient databases of C_{lv} and C_m . The presently available C_{lv} and C_m databases are obtained from laboratory experiments under restricted conditions. Limitations arise from not taking into account the effects of not allowing in-line (IL) motion (the effect of IL motion on CF motion) and the effect of high Reynolds number not achieved in a laboratory environment.

Mukundan et al. (2009) has evolved a method to improve the theoretical estimates of $Y_n(z)$ and ω_n using a database correction algorithm. This method poses the problem of correcting the databases as a parameter estimation problem where the C_{lv} and C_m databases are parameterized using a set of carefully chosen parameters \vec{p} . These parameters are then systematically varied to obtain modified versions of the existing C_{lv} and C_m databases. Use of these parameterized C_{lv} and C_m databases makes the theoretical estimates of $Y_n(z)$ and ω_n a function of the parameters \vec{p} . These theoretical estimates (denoted by $Y_{n-th}(z; \vec{p})$ and $\omega_{n-th}(\vec{p})$) using the modified databases are compared with the experimental observations (denoted by $Y_{n-exp}(z; \vec{p})$ and $\omega_{n-exp}(\vec{p})$) and the error between them are minimized. In the following section, we describe the database correction method specifically tailored for the reconstruction problem where the theoretical estimates are compared with experimental measurements at the sensor locations. The overall algorithm is illustrated as a flowchart depicted in Fig. 4 and the various parts of the algorithm are briefly described below.

Experimental measurements. The acceleration signals $a_{exp}(z_s, t)$ at the sensor locations are used to obtain the displacement signals $y_{exp}(z_s, t)$. The Fourier transform of the signals are taken with respect to time. We identify the peak

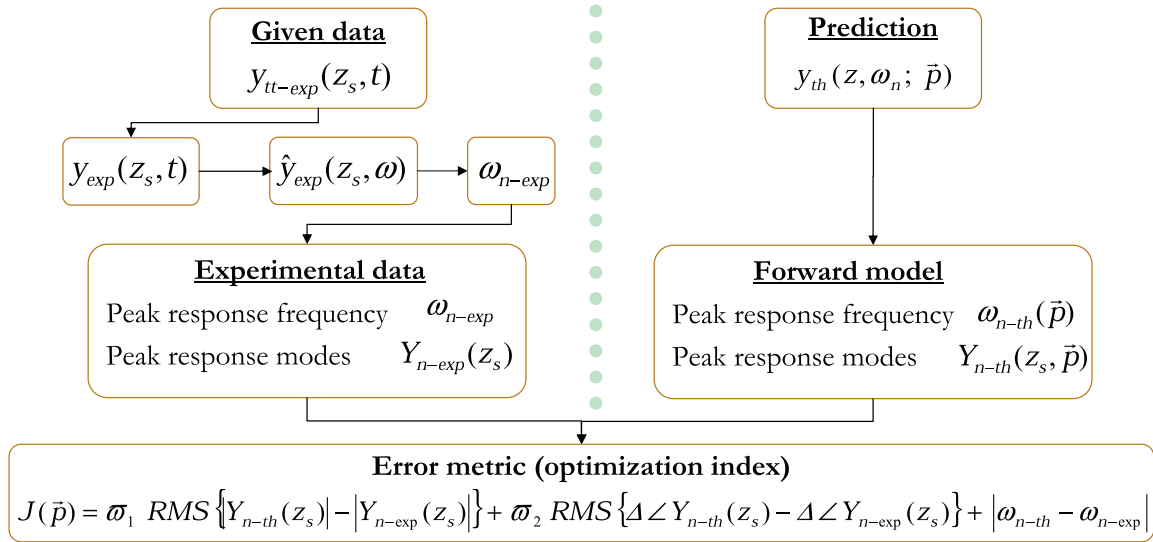


Fig. 4. Overview of the method used for local lift coefficient database correction.

response frequency ω_{n-exp} first, and then corresponding to the ω_{n-exp} , we extract the peak response modes at the sensor location $Y_{n-exp}(z_s)$. Thus the experimental data consists of ω_{n-exp} and $Y_{n-exp}(z_s)$. For a detailed reference on obtaining the peak response modes and peak response frequencies from experimental data refer to Mukundan (2008).

Parameterized theoretical estimates. The C_{lv} and C_m databases are parameterized using 12 parameters (denoted by \bar{p}) as mentioned in Mukundan et al. (2009). These 12 parameters correspond to a fine balance involving a minimal number of parameters and the adequate representation of the C_{lv} and C_m databases. Depending on the situation at hand, we may employ a reduced set of parameters for adequately representing the C_{lv} and C_m databases. Given the flow profile $U(z)$, and the lift coefficient databases of C_m and C_{lv} , the theoretical estimates of peak response frequencies ω_{n-th} and peak response modes $Y_{n-th}(z)$ are obtained by solving the nonlinear eigenvalue problem (for details refer to Triantafyllou (1998)) given by

$$\left\{ -\omega^2 \left[m + C_m \left(\rho_f \frac{\pi D^2}{4} \right) \right] + i\omega b \right\} Y - \frac{\partial}{\partial z} \left(T \frac{\partial Y}{\partial z} \right) + \frac{\partial^2}{\partial z^2} \left(EI \frac{\partial^2 Y}{\partial z^2} \right) = iC_{lv} \left(\frac{\rho_f U^2}{2} D \right) \frac{Y}{|Y|} \quad (12)$$

where ρ_f is the density of the fluid, m is the linear mass density, T is the tension and EI is the bending rigidity of the riser under consideration. The above Eq. (12) with the appropriate boundary conditions represents the *nonlinear eigenvalue problem*. The nonlinearity arises from the presence of terms like $Y(z)/|Y(z)|$, C_m and C_{lv} which depend on Y and ω . For obtaining the theoretical estimates $Y_{n-th}(z; \bar{p})$ and $\omega_{n-th}(\bar{p})$ we once again use the empirical prediction program VIVA (Triantafyllou, 2006). This is followed by extracting the peak response modes $Y_{n-th}(z_s; \bar{p})$ at the sensor locations z_s .

Error metric (optimization index). As discussed with great detail in Mukundan et al. (2009), the important observables in a VIV problem are the peak response frequency, the modal magnitude and the modal phase angle of the peak response mode. As a result, we need to develop an error metric to capture these three aspects of riser VIV response. It is to be emphasized that for the reconstruction problem both modal magnitude and modal phase angle are important. Based on this we choose the *optimization index* or *error metric* in the following form as

$$J(\bar{p}) = \varpi_1 \text{rms} \{ |Y_{n-th}(z_s, \bar{p})| - |Y_{n-exp}(z_s)| \} + \varpi_2 \text{rms} \{ |\Delta Y_{n-th}(z_s, \bar{p}) - \Delta Y_{n-exp}(z_s)| \} + |\omega_{n-th}(\bar{p}) - \omega_{n-exp}|, \quad (13)$$

where ϖ_1, ϖ_2 are factors which allows us to weigh the relative importance of minimizing error in the modal magnitude, the modal phase angle and the peak response frequency. The notation $\Delta Y_{n-exp}(z_s) = Y_{n-exp}(z_{s+1}) - Y_{n-exp}(z_s)$ represents the difference in modal phase angle between two consecutive sensors.

Solution technique. The large number of parameters in \bar{p} (12 in number) renders *grid search* or *random search* methods computationally impossible. Our choice of error metric $J(\bar{p})$ is highly nonlinear and involves several heuristics which makes it discontinuous. As a result, *gradient based* or *quasi Newton* methods will not work. As a result the parameter estimation problem is solved using a directed random search algorithm called *simulated annealing method* due to its simplicity and speed (Morgan and Rao, 2006). This algorithm is described in more detail in Mukundan et al. (2009).

The input to a simulated annealing algorithm is a range for each parameter within which the solution is expected to lie, and the output is the parameter-set \vec{p}_{opt} which minimizes the error metric over the parameter range.

The result from such an optimization method is the recalibrated C_{lv} and C_m databases whose use during prediction will minimize the error between the observed experimental measurements and the theoretical estimates at the sensor locations only. In this paper, the local lift coefficient calibration method is described primarily from a reconstruction view point. One may also evolve methods to use the data from a few sensors (especially from full scale data) to improve the predictive capabilities for real world applications. Such a method is however not within the purview of this paper.

5. Experimental data: Norwegian deepwater programme high mode VIV tests

The experimental data used in this paper to validate the reconstruction methods are from the high mode VIV experiments sponsored by the Norwegian Deepwater Programme (NDP). For a detailed description of the experiments refer to Braaten and Lie (2004) and Trim et al. (2005). The riser model is made of fiber glass and had a length $L = 38$ m, diameter $D = 0.027$ m, linear mass density in air $m = 0.761$ kg m⁻¹, tension $T = 4000$ – 6000 N (for running VIVA $T = 5000$ N was assumed) and bending stiffness $EI = 37.2$ N m². The riser model was taut horizontally and towed in water at different speeds. If both ends of the riser is towed simultaneously at a constant velocity U_{max} , we obtain a uniform flow profile of the form $U(z) = U_{\text{max}}$. Towing only one end of the riser at a velocity U_{max} in a predefined arc while keeping the other end at rest results in a triangular sheared flow profile of the form $U(z) = U_{\text{max}}(1-z/L)$. Datasets with numbers between 2010 and 2220 correspond to a uniform profile, and datasets with numbers between 2310 and 2520 correspond to a linearly sheared flow profile. The riser was instrumented using 24 strain gauges and 8 accelerometers in the CF direction, while the motion in IL direction was observed using 40 strain gauges and 8 accelerometers. These sensors measure data at a constant time sampling rate equal to 1200 Hz.

For the application of reconstruction method for the case of large number of sensors, we utilize data from all these sensors. Application of reconstruction method for the case of few sensors on the other hand, utilizes the data from some or all of the 8 accelerometers only.

6. Applications

We apply the reconstruction methods to data from NDP experiments (refer to Section 5). To understand and verify the accuracy, speed and limitations of the reconstruction methods, we apply them first to benchmark data which is constructed synthetically using simulated riser VIV displacements known a priori. Applications using the reconstruction method for large number of sensors is presented in Section 6.1, while Section 6.2 presents application of the reconstruction method using data from few sensors.

6.1. Application of reconstruction method using data from large number of sensors

The reconstruction method for the case of large number of sensors is first applied to benchmark data in Section 6.1.1. This will be followed by the application of our method to data from NDP experiments in Section 6.1.2.

6.1.1. Application to benchmark data

The benchmark data was created for a riser with properties similar to that of the NDP riser model (described in Section 5). We aim at showing that for the benchmark case, the use of sines and cosines will result in excellent accuracy during the reconstruction. Displacements are simulated by choosing one of the complex peak response modes $Y_c(z)$ obtained for a linearly sheared profile from VIVA, and using the formula $y(z, t) = \text{Re}\{Y_c(z)\eta_c(t)\}$ where, $Y_c(z)$ is the chosen VIVA mode and $\eta_c(t)$ is a narrow banded function comprising of 5 frequencies centered around the modal frequency f_c corresponding to $Y_c(z)$. $\eta_c(t)$ is obtained as $\eta_c(t) = \sum_{j=1}^5 a_j e^{i(2\pi f_j t + \phi_j)}$ where, $a_j = [0.05 \ 0.20 \ 1.00 \ 0.20 \ 0.05]$, $f_j = [0.98 \ 0.99 \ 1.00 \ 1.01 \ 1.02]$ and ϕ_j are randomly chosen. Since the idea is to simulate a typical NDP dataset, from simulated displacements we extract accelerations at the NDP accelerometer locations (8 in number) and strains at the NDP strain gauge locations (24 in number). Thus the benchmark dataset consisted of 24 strain signals and 8 accelerometer signals all sampled at 1200 Hz (corresponding to sampling frequency in NDP data).

We apply the reconstruction methodology to the benchmark dataset using the data from all the 32 sensors (24 strain gauges and 8 accelerometers). The resulting displacements from the reconstruction closely matches the original displacements for the benchmark datasets considered, and such excellent behavior is repeated for several other

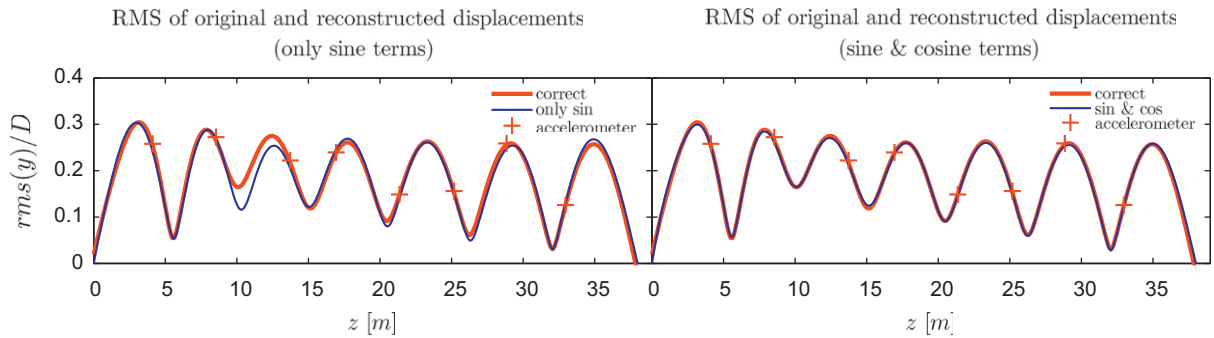


Fig. 5. Comparison of the rms of the original and reconstructed displacements for the benchmark data using only sine terms (*left*) and using both sine and cosine terms (*right*). The + sign represents the displacements from acceleration signals at the accelerometer locations. Note the deviations observed in the reconstruction using only sine terms.

benchmark datasets which were similarly created. The reconstruction is accurate not only at the sensor locations but over the entire riser. Specifically to illustrate the importance of cosine terms (previously considered unnecessary) we perform two separate reconstructions and the root mean square (rms) of the reconstructed and the original signals are studied in Fig. 5, as follows.

Using only sine terms. As depicted in Fig. 5 (*left*), there is noticeable deviation between the rms of the original signal and the rms of the reconstructed displacements over a large part of the riser. For this example we have utilized 17 sine terms. Use of increased number of spatial harmonics (increased number N_m) does not solve this problem. The reconstruction using increased number of sine terms converges but converges to the wrong solution.

Using both cosine and sine terms. As depicted in Fig. 5 (*right*), the reconstruction closely matches the original over the entire riser. For this reconstruction, we utilized 11 sine terms and 14 cosine terms. Similar results were observed for several benchmark datasets and the results illustrate the importance of using both sine and cosine terms for accurately reconstructing the riser VIV motions. As mentioned previously, the riser motions arising from VIV consist of traveling waves arising from nonlinear interaction between the riser and the fluid. This will result in boundary layers close to the riser ends yielding sharp jumps in curvature. As a result, problems are introduced during decomposition of riser VIV motions using sine terms alone due to interpolation of the curvatures in addition to accelerations, but produces better results when both sine and cosine terms are used.

6.1.2. Application to experimental data from NDP

The application of reconstruction to several benchmark tests gives us confidence to apply the method to NDP experimental data. The number of sensors employed in NDP experiment (32 in CF and 48 in IL) is expected to allow the reconstruction of the harmonic part of the CF motion and the second harmonic part (twice the Strouhal frequency) of the IL motion. Fig. 6 depicts the typical comparison of the original and reconstructed curvature signals at few chosen locations along the riser for datasets 2350 with $U_{\max} = 0.7 \text{ m s}^{-1}$ (columns I and II) and 2420 with $U_{\max} = 1.4 \text{ m s}^{-1}$ (columns III and IV), respectively. These figures clearly illustrate how the reconstruction closely resembles the experimental data at least at the sensor locations.

Another good way to observe the riser VIV motions are to view it as an animation. We present several frames (corresponding to approximately one half cycle) depicting motion of the riser for NDP dataset 2350 with $U_{\max} = 0.7 \text{ m s}^{-1}$ (linearly sheared flow profile) in Fig. 7(a) and NDP dataset 2050 with $U_{\max} = 0.7 \text{ m s}^{-1}$ (uniform flow profile) in Fig. 7(b). One significant finding is the presence of traveling waves present in the riser VIV response. Traveling waves in riser VIV response was also observed and cited by Lie and Kaasen (2006). Linearly sheared flows clearly depict disturbances (pulses) in CF displacements which travel along the entire length of the riser with directional consistency. The presence of traveling waves can be noticed by following the location of the nodes (or crests or troughs) in the displaced shape of the riser for various time steps as shown in Fig. 7(a). Our observations over several linearly sheared current profiles [refer to Mukundan (2008)] show that as flow velocity increases, the presence of traveling waves become more apparent due to increased number of pulses generated in each second. CF displacements for uniform flow on the other hand depict disturbances which propagate over a part of the riser length with no directional consistency. Also observed is the presence of standing waves whose shapes differ significantly from the purely sinusoidal free

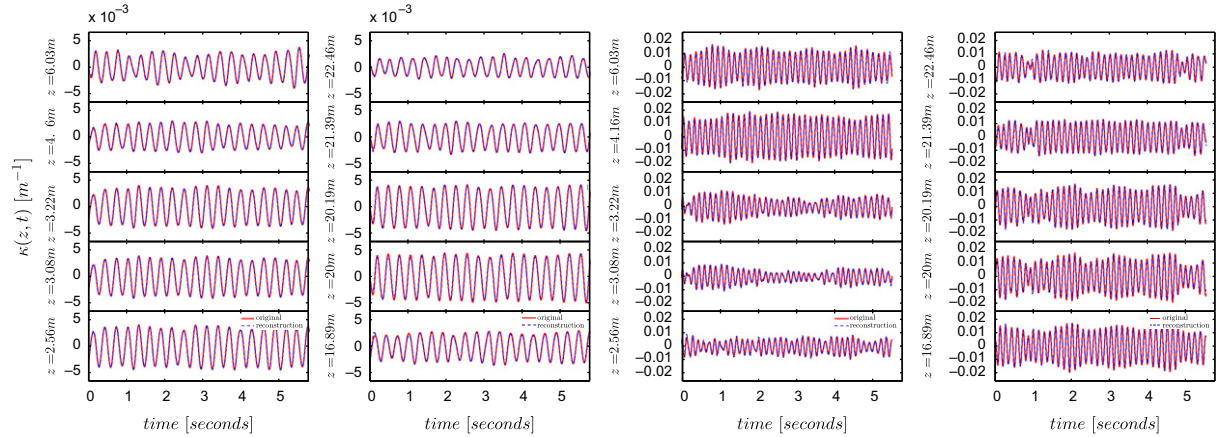


Fig. 6. Comparison of the CF experimental curvature time series (red), and the reconstructed CF curvature time series (blue) at select strain gauge locations for NDP dataset 2350 with $U_{\max} = 0.7 \text{ m s}^{-1}$ (columns I and II). Comparison of the CF experimental curvature time series (red), and the reconstructed CF curvature time series (blue) at select strain gauge locations for NDP dataset 2440 with $U_{\max} = 1.4 \text{ m s}^{-1}$ (columns III and IV). Note that the reconstructed curvature closely matches the experimental data at the sensor locations. (For interpretation of the references to colour in this figure legend, the reader is referred to the web version of this article.)

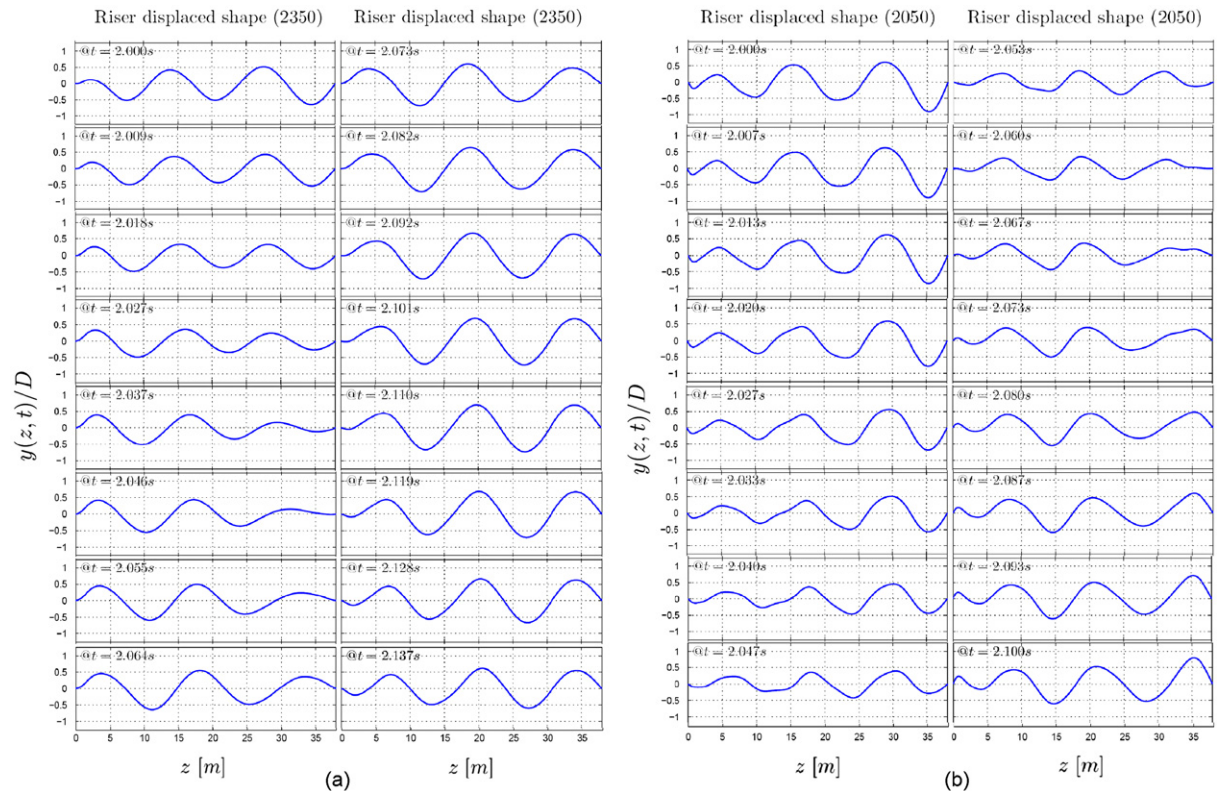


Fig. 7. Depicts the displaced shape of the riser (after reconstruction) at several instances of time for (a) NDP dataset 2350 with $U_{\max} = 0.7 \text{ m s}^{-1}$ corresponding to a triangular sheared flow profile and (b) NDP dataset 2050 with $U_{\max} = 0.7 \text{ m s}^{-1}$ corresponding to a uniform flow profile. One can clearly observe the presence of disturbances which starts around $z = 0$ and moves along the riser for the sheared case while we observe that the displaced shape of the riser for uniform profile is not a standing wave pattern.

vibration modes predicted by state-of-art prediction programs for uniform flow profiles. In fact, this phenomenon could be a case where the observed standing wave may be combination of several purely sinusoidal modes with their corresponding modal frequency converging to a single value (frequency coalescence).

6.2. Application of reconstruction method using data from few number of sensors

We aim at applying our reconstruction method for the case involving data from only a few sensors. As mentioned previously, the method requires accurate prediction of the riser peak response modes and peak response frequencies. So we will first consider a case where we know accurately the peak response modes and frequencies and show that the methodology works and that the reconstruction is accurate (a benchmark example). This will be followed by an application of the method to NDP experimental data using the prediction schemes presently available. This will also include a database correction scheme for improving the prediction accuracy at least at the sensor locations. Specifically we will show the results for NDP dataset 2430 corresponding to a triangular flow profile with a maximum velocity $U_{\max} = 1.5 \text{ m s}^{-1}$. For comparing the accuracy of the reconstruction from this method, we will always compare it with reconstructed response from the scenario where data from a large number of sensors are used.

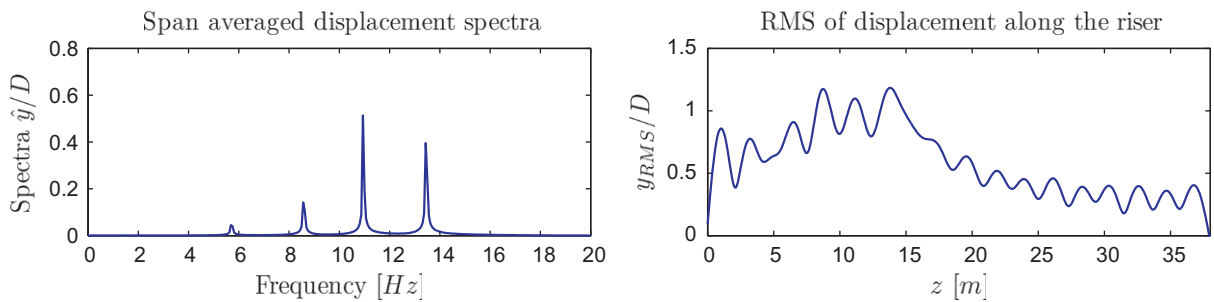


Fig. 8. Left: the span-averaged spectrum of the benchmark data; right: the rms of the displacements measured along the riser.

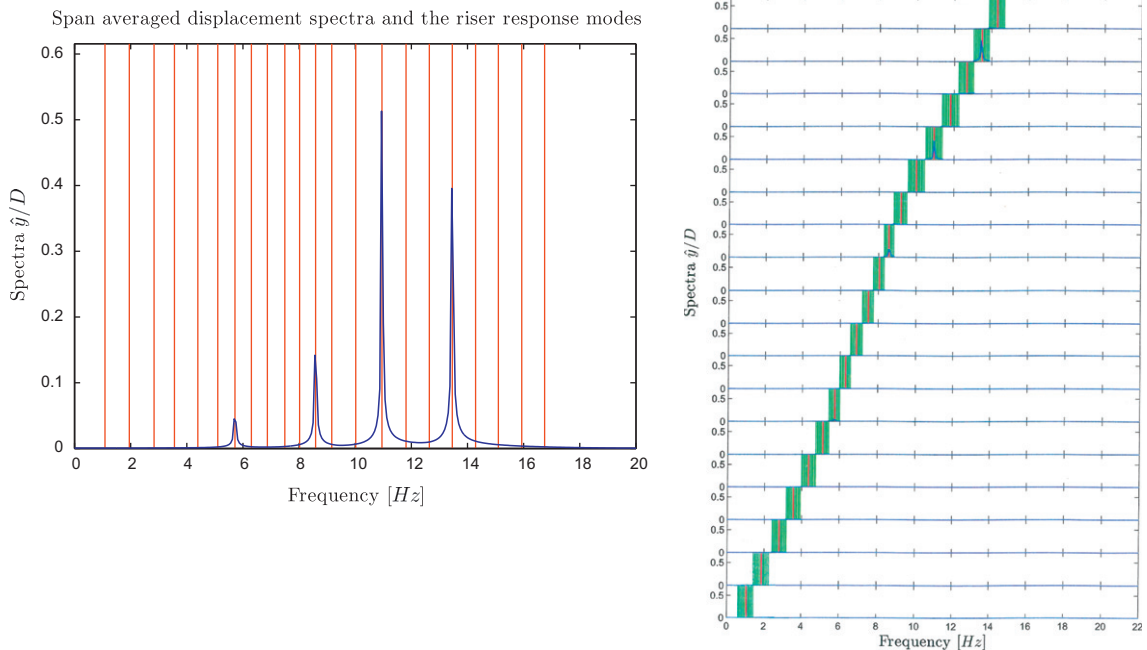


Fig. 9. Left: the span-averaged spectra of the benchmark data. The vertical lines represents the VIVA predicted ω_n . Right: the spectra of sensor signals $\hat{y}(z_s, \omega)$ are subdivided by bandpass filtering them around each ω_n to obtain N_m separate spectra $\hat{y}_{n\text{-filt}}(z_s, \omega)$.

6.2.1. Application to benchmark data

To validate the algorithm, we apply the developed methodology to a benchmark dataset constructed synthetically. The benchmark data corresponds to a riser with properties similar to that of the NDP riser described in Section 5. The riser encounters a triangular flow profile $U(z) = U_{\max}(1-z/L)$ corresponding to a maximum flow velocity $U_{\max} = 1.5 \text{ m s}^{-1}$. Corresponding to the above riser and flow properties, VIVA produced peak response modes $Y_n(z)$ and peak response frequencies ω_n are utilized to produce the displacements as $y(z, t) = \text{Re}\{\sum_{n=1}^{N_m} c_n Y_n(z) e^{i\omega_n t}\}$, where coefficients c_n are chosen so as to produce a riser displacements where select number of frequencies (4 frequencies) participate. Accelerations are extracted for a variety of cases involving different number of sensors N_s , located at the corresponding sensor location z_s . The resultant acceleration signals are around 16 s in time, and as shown in Fig. 8 (left) have four primary peaks depicting a multi-frequency response. For the reconstruction algorithm, in addition to the acceleration data, we are also given the flow profile $U(z)$ from which we can obtain $Y_n(z)$ and ω_n using VIVA.

For this benchmark example, VIVA produced 22 peak response frequencies and peak response modes. Fig. 9 illustrates how we subdivide the spectrum of a signal into several spectra each corresponding to the given ω_n . The rms of the original signal and the reconstructed signals for two N_s cases are presented in Fig. 10 ($N_s = 2$ and 4). Note that we do not expect to have 4 sensors for a dataset with 4 frequency components.

As seen from Figs. 10, the reconstruction is quite accurate even for number of sensors as low as 2. The comparison of the original and the reconstructed signals at the sensors locations also depict excellent agreement. It was found that the reconstruction depends on (i) the sensor locations (z_s), and (ii) the number of sensors (N_s). A more uniform distribution of sensors yields a more accurate reconstruction. Another observation is the fact that accurate reconstruction depends heavily on the accuracy with which we can obtain $Y_n(z)$ and ω_n . Our predictive capabilities could be compromised due to the minor errors in measuring the flow profile or the empirical lift coefficient databases. Thus the illustrative examples clearly show that accurate reconstruction is possible even for very small N_s , provided we are able to accurately evaluate $Y_n(z)$ and ω_n .

Sensitivity to flow profile. As mentioned previously, the peak response modes $Y_n(z)$ and peak response frequencies ω_n are not the classical free vibration modes and frequencies and hence depend critically on the flow profile $U(z)$. Thus a reconstruction employing $Y_n(z)$ and ω_n also depends on $U(z)$. If there is an inaccuracy in obtaining the flow profile, the accuracy of reconstruction may be affected. The sensitivity of the flow profile on the reconstruction is studied using the benchmark example. The benchmark data remains the same but we use a slightly perturbed flow profile while performing the reconstruction. The perturbed flow profile is again a linearly sheared profile but given by: $U_p(z) = [U_{\max} + \Delta U_{\max}](1-z/L)$, where ΔU_{\max} is the error assumed to be introduced while measuring the flow profile.

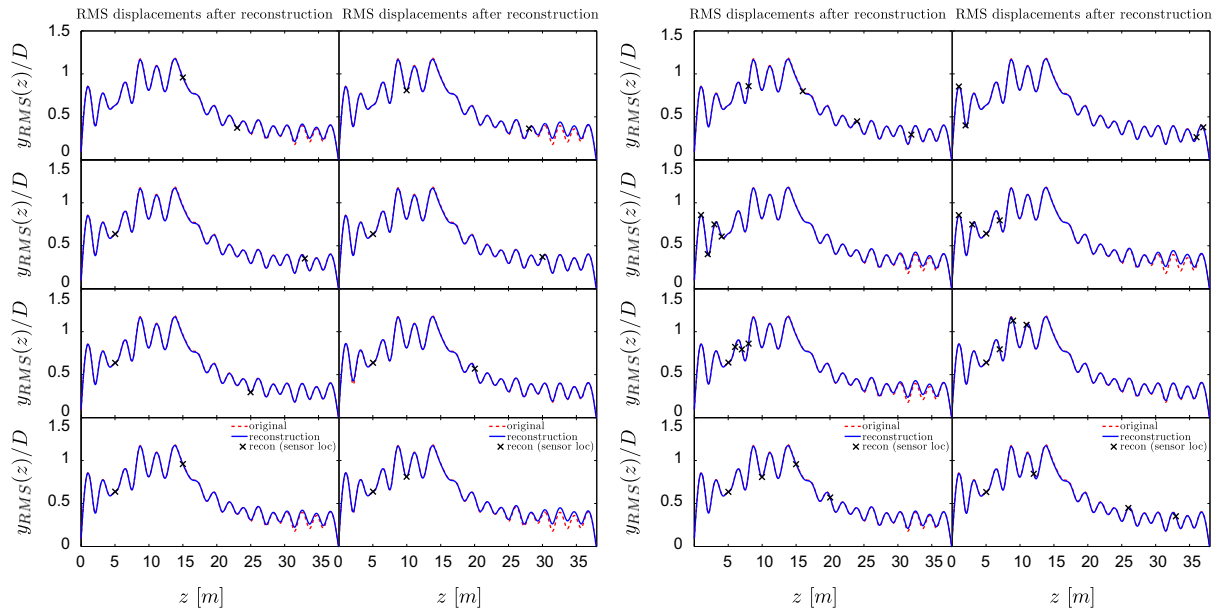


Fig. 10. Results comparing the rms of the original and the reconstructed signals obtained using the proposed reconstruction algorithm for benchmark data. Various cases of sensor locations (marked by the 'x' sign) for number of sensors $N_s = 2$ (left) and $N_s = 4$ (right) are illustrated.

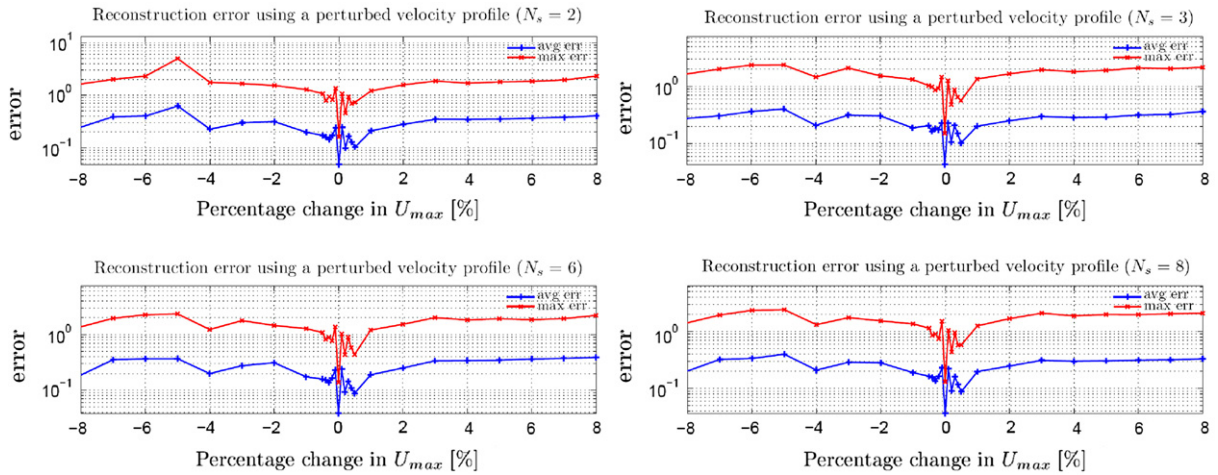


Fig. 11. Depicts the average and maximum reconstruction error as a function of the relative error $\Delta U_{max}/U_{max}$ in the flow profile used to obtain $Y_n(z)$ and ω_n for various N_s cases. We can observe that the accuracy of reconstructed response is highly sensitive to the error in the flow profile used during reconstruction.

The $Y_n(z)$ and ω_n corresponding to various such perturbed flow profiles $U_p(z)$ are obtained, and used to reconstruct the data corresponding to a flow profile $U(z) = U_{max}(1 - z/L)$.

We measure the reconstruction error (*average error* and *maximum error*)² corresponding to different values of the relative error in the flow profile $\Delta U_{max}/U_{max}$. Fig. 11 quantifies the sensitivity of the reconstruction method for perturbations in the flow profile for various number of sensors N_s placed uniformly along the riser.

As observed from Fig. 11, for up to 4% relative error in U_{max} , the average error is less than 0.4, while the maximum error is around 1 for various cases of N_s . This means that the riser responses may differ by as much as one diameter in the worst case scenario when the original and the reconstructed riser motions are out of phase at some location at an instance in time. For each choice of N_s , we can observe that the reconstruction errors become zero when the relative error in the flow profile becomes zero. For small errors in the flow profile, the reconstruction error is small but grows considerably as the error in the flow profile grows. This clearly indicates the necessity of accurately obtaining the flow profile in addition to accurately obtaining the riser VIV measurements.

6.2.2. Application to experimental data from NDP (employing the VIVA generated modes and frequencies)

We apply the reconstruction method to NDP dataset 2430 corresponding to the flow profile $U(z) = 1.5(1 - z/L) \text{ m s}^{-1}$. Next, we use VIVA to generate the $Y_n(z)$ and ω_n corresponding to the flow profile $U(z)$. The existing C_{lv} and C_m databases are used by VIVA to obtain the $Y_n(z)$ and ω_n . As discussed previously, observations from prediction using the existing C_{lv} and C_m databases lead to large under estimations and over estimations. This is because of the inaccuracy in predicting ω_n and $Y_n(z)$ (both magnitude and phase of $Y_n(z)$) resulting from the use of the existing C_{lv} and C_m databases.

To correct this situation, we employ the local lift coefficient correction algorithm using data from 8 accelerometers. The result from such a database correction method is illustrated in Fig. 12. Fig. 12 (left) shows the comparison of $Y_n(z)$ and ω_n using the existing databases, while Fig. 12 (right) shows the comparison using the optimal databases. The modified $Y_n(z)$ and ω_n obtained using the optimal databases are used for reconstruction. The results are shown in Figs. 13 from which we can observe that the reconstruction method depicts reasonably good agreement for various cases of number of sensors N_s and sensor placements z_s . As observed from Fig. 13 there is a consistent under prediction at the hotspot close to the riser end (near $z = 0$). We attribute this to the limitations in the present theoretical models which even with improved C_{lv} and C_m databases cannot take into account the significant traveling waves in riser VIV. The increased amplitude leads to increased damping and increased dissipation of energy to support traveling waves.

Using the data from 8 accelerometers available in the NDP data, we obtain the reconstruction for all the combinations of number of sensors taking N_s sensors at a time located at the sensor locations z_s . The error between the reconstructed signal using few sensors and the original signal (using all the available sensors using the method described

²The two nondimensional reconstruction error metrics are (i) average error = $(1/(D LT)) \int \int |y_{orig}(z, t) - y_{recon}(z, t)| dt dz$, and (ii) maximum error = $(1/D) \max(|y_{orig}(z, t) - y_{recon}(z, t)|)$, where T is the time interval over which we perform the reconstruction, $y_{orig}(z, t)$ is the original riser response and $y_{recon}(z, t)$ is the reconstructed riser response.

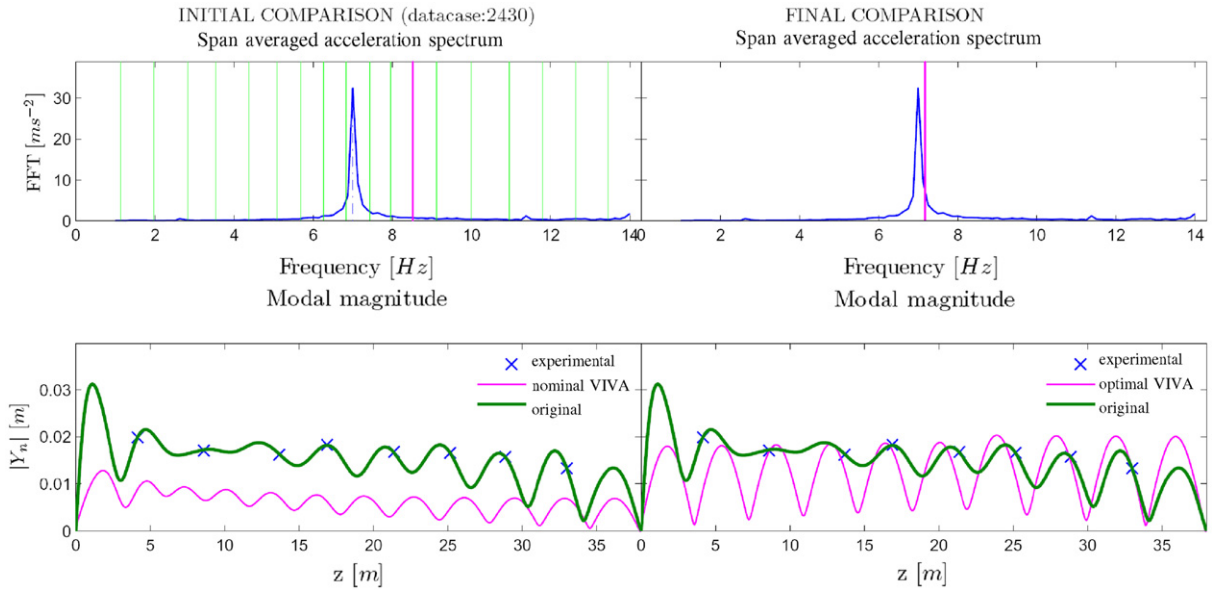


Fig. 12. Application of the local lift coefficient extraction method to NDP dataset 2430 corresponding to a linearly sheared current profile with $U_{\max} = 1.5 \text{ m s}^{-1}$. *Left*: comparison of the experimental and nominal theoretical prediction; *right*: comparison of the optimal and experimental prediction. Note that with the use of the recalibrated C_{lv} and C_m databases, the error between experiments and the theoretical estimates at the sensor locations (\times sign) are significantly reduced.

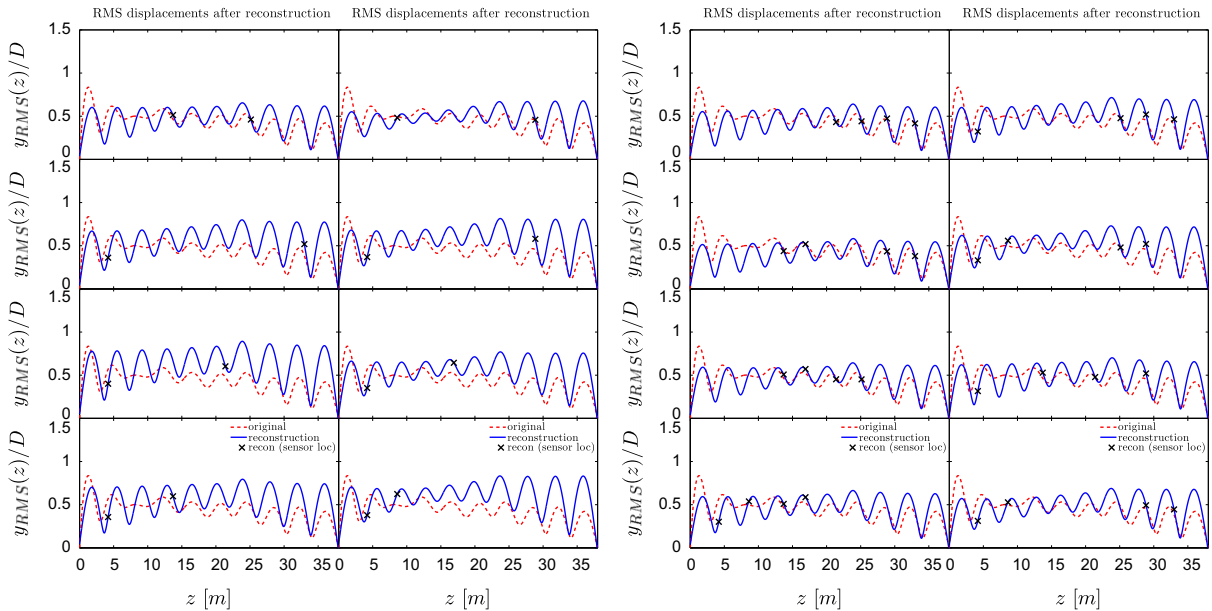


Fig. 13. Results comparing the rms of the original and reconstructed signals (using corrected lift coefficient databases) for NDP dataset 2430 with $U_{\max} = 1.5 \text{ m s}^{-1}$ when the number of sensors $N_s = 2$ (*left*) and $N_s = 4$ (*right*) for various combinations of sensor locations. The locations of the sensors are marked by the ‘ \times ’ sign.

in Section 2) is obtained. Fig. 14 illustrates how the average error vary as a function of number of sensors N_s . For the use of a small number of sensors, there is a large variability in the reconstruction error. In addition, the maximum value of the average error is as high as 35%. As the number of sensors increase, the maximum value of the average reconstruction error and the variability in the average reconstruction error both decreases. Physically it means that the

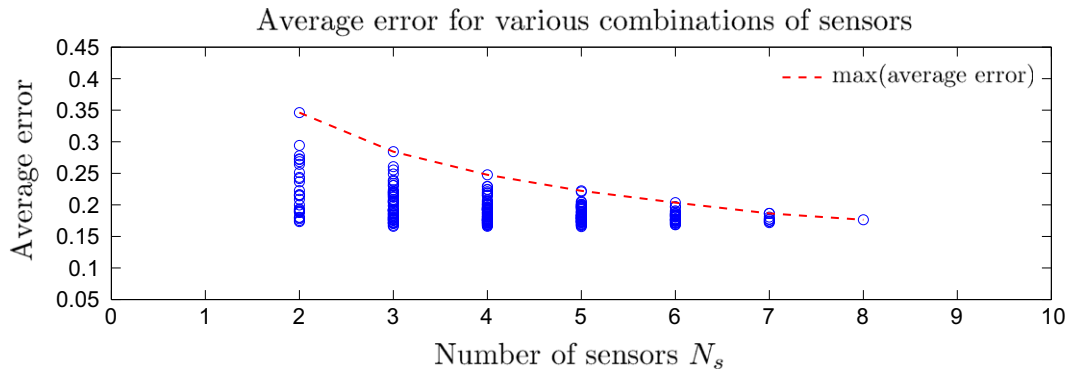


Fig. 14. The average error during reconstruction for all possible combinations using data from N_s sensors from a maximum of the 8 accelerometers for NDP dataset 2430 corresponding to a linearly sheared current profile with $U_{\max} = 1.5 \text{ m s}^{-1}$.

confidence in our reconstruction increases with the use of increasing number of sensors. In addition, it was also observed that a more uniform distribution of sensors placed along the riser provides more accurate reconstruction.

7. A study of reconstruction error

In the previous sections we describe the reconstruction methods for use with a large number of sensors and with few number of sensors. Such reconstruction methods are useful only if we can provide associated error metrics which provides us some confidence on the reconstruction accuracy. In this section we present our effort to quantify the error that might have crept in during the reconstruction method for the case of large number of sensors outlined in the Section 2. The accuracy of the reconstruction may be compromised due to three major reasons:

- (i) uncertainty from the presence of noise in experimental data; this includes the presence of noise in experimental data like the sensor noise, or noise arising from the setup of the experimental apparatus;
- (ii) uncertainty from the use of a finite number of sine and cosine terms during reconstruction; this considers the adequateness of the reconstruction basis (sine and cosine terms) to represent the riser VIV motions;
- (iii) uncertainty from the presence of both acceleration and strain measurements; this considers the fact that in a realistic situation, the acceleration and curvatures (strains) may have completely different magnitudes (depending primarily of the length of the riser) potentially resulting in numerical issues during reconstruction.

We perform a systematic study to quantify each of the sources of uncertainty (error) followed by an effort to quantify the cumulative error from each of these sources of uncertainty.

7.1. Uncertainty from the presence of noise in experimental data

In this section we will discuss how we can quantify the uncertainty in reconstruction arising from the presence of noise in the experimental data. The noise may be due to the sensors themselves or may arise from the experimental setup. Lie and Kaasen (2006) presents a method to identify the reconstruction error by propagating the noise in data to the variability in the modal participation factors based on their reconstruction using classical eigenmodes. Additionally, they consider only the variance terms while ignoring the covariance terms during reconstruction error estimation, resulting in significant increase in the error bound estimates. We extend and improve the methodology to apply it to our reconstruction method involving Fourier decomposition. In addition, we also consider not only the variance terms but also the covariance terms.

We assume that the measured experimental data $y_e(z_s, t)$ consists of the actual experimental data $y(z_s, t)$ with some noise $n(z_s, t)$, where z_s corresponds to the location of the sensors as

$$y_e(z_s, t) = y(z_s, t) + n(z_s, t), \quad (14)$$

The above system of equations can be written in a matrix form as $\mathbf{Y}_e = \mathbf{Y} + \mathbf{N}$, which in frequency domain can be written as $\hat{\mathbf{Y}}_e = \hat{\mathbf{Y}} + \hat{\mathbf{N}}$. The noise terms $n(z_s, t)$ in each sensor signal are assumed to be independent, Gaussian white

noise with a zero mean and a standard deviation σ_n . Standard deviation is usually expressed as percentage of the signal strength. For simplicity, we non-dimensionalize standard deviation using the riser diameter (typical response amplitude) as $\sigma_n = D\sigma_{\bar{n}}$. The uncertainty arising from noise propagates to our estimation of $\hat{\mathbf{w}}$ (or \mathbf{w}). If we write $\hat{\mathbf{Y}}_e = \Phi\hat{\mathbf{w}}_e$, and $\hat{\mathbf{Y}} = \Phi\hat{\mathbf{w}}$, where $\hat{\mathbf{w}}_e$ is the estimate using noisy data and $\hat{\mathbf{w}}$ is the actual one, then we can write $\hat{\mathbf{Y}}_e = \hat{\mathbf{Y}} + \hat{\mathbf{N}}$ as

$$\Phi\hat{\mathbf{w}}_e = \Phi\hat{\mathbf{w}} + \hat{\mathbf{N}}. \quad (15)$$

Premultiplying the above Eq. (15) using the pseudo-inverse Φ^+ we obtain $\hat{\mathbf{w}}_e = \hat{\mathbf{w}} + \Phi^+ \hat{\mathbf{N}}$, or $\hat{\mathbf{w}}_e = \hat{\mathbf{w}} + \hat{\mathbf{e}}_w$, where $\hat{\mathbf{e}}_w \equiv \Phi^+ \hat{\mathbf{N}}$ which in the time domain can be written as $\mathbf{e}_w = \Phi^+ \mathbf{N}$. \mathbf{e}_w is the error in estimating \mathbf{w} , and can be quantified using the covariance matrix \mathbf{E}_w . The covariance matrix \mathbf{E}_w of the error in estimating \mathbf{w} can then be written as: $\mathbf{E}_w = \mathbb{E}\{\mathbf{e}_w \mathbf{e}_w^T\} = \sigma_n^2 \Phi^+ (\Phi^+)^T$, where $\mathbb{E}\{\}$ is the expectation operator. Using \mathbf{E}_w , we can propagate the error in estimating \mathbf{w} to the error in estimating the displacement $y(z,t)$ using Eq. (2) which can be written in an expanded form as

$$y(z,t) = \phi_1(z)w_1(t) + \phi_2(z)w_2(t) + \dots + \phi_i(z)w_i(t) + \dots + \phi_N(z)w_N(t). \quad (16)$$

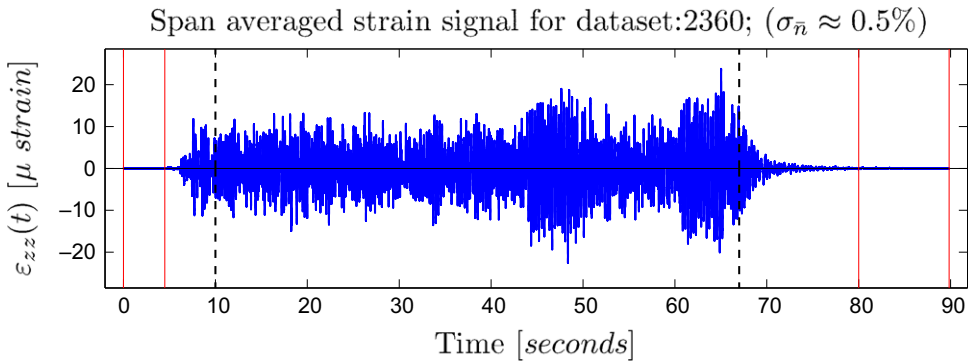


Fig. 15. The span-averaged strain signal from NDP dataset 2360 with $U_{\max} = 0.8 \text{ m s}^{-1}$ is subdivided into three segments. Segments within the solid red vertical lines correspond to zero flow velocity periods, and the segments between the dashed black vertical lines correspond to the period when the riser was towed. Note that for calculating the $\sigma_{\bar{n}}$ we took the absolute value of all the CF strain measurements and then took the average along the span. The $\sigma_{\bar{n}}$ level can be obtained from the ratio of rms of the zero velocity signal and rms of the actual VIV signal. (For interpretation of the references to colour in this figure legend, the reader is referred to the web version of this article.)

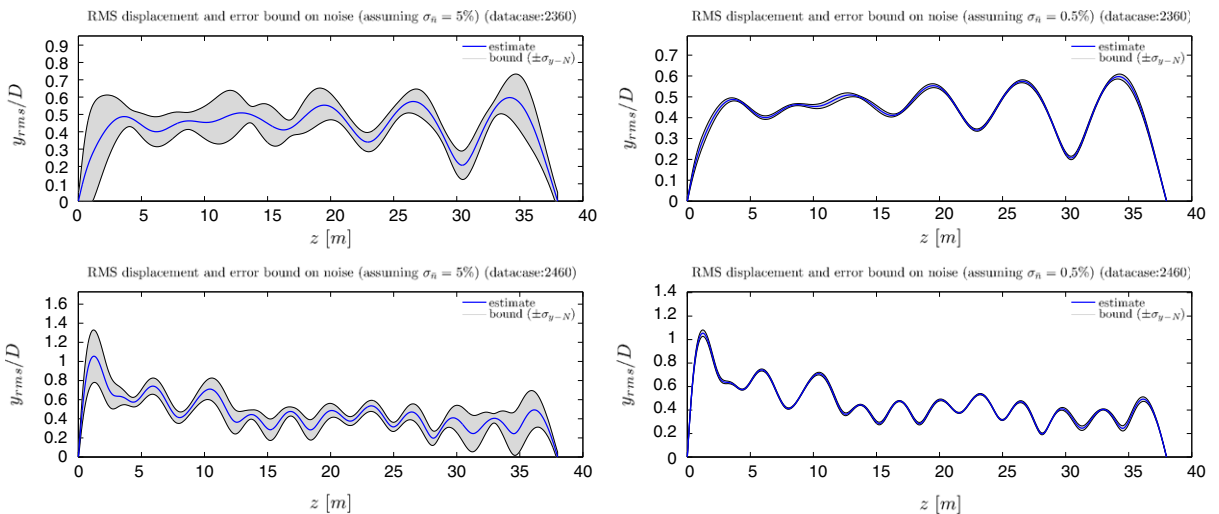


Fig. 16. Variability in reconstruction arising due to the presence of noise in experimental measurements. Rms displacement and error bound assuming $\sigma_{\bar{n}} = 5\%$ (top left) and $\sigma_{\bar{n}} = 0.5\%$ (top right) for NDP dataset 2360 ($U_{\max} = 0.8 \text{ m s}^{-1}$). Rms displacement and error bound assuming $\sigma_{\bar{n}} = 5\%$ (bottom left) and $\sigma_{\bar{n}} = 0.5\%$ (bottom right) for NDP dataset 2460 ($U_{\max} = 1.8 \text{ m s}^{-1}$).

Note that $w_i(t)$ are not independent, and hence both the variance and covariance terms of \mathbf{E}_w are important. The variance of the displacement error due to noise in the experimental data at any location z along the riser $\sigma_{y-N}^2(z)$ can then be obtained as $\sigma_{y-N}^2(z) = \mathbf{P}(z)\mathbf{E}_w\mathbf{P}(z)^T$, where $\mathbf{P}(z) = [\phi_1(z)\phi_2(z)\dots\phi_N(z)]$. Using expressions for \mathbf{E}_w while expanding for $\sigma_{y-N}^2(z)$ we obtain

$$\sigma_{y-N}^2(z) = \sigma_n^2\mathbf{P}(z)\mathbf{\Phi}^+(\mathbf{\Phi}^+)^T\mathbf{P}(z)^T, \tag{17}$$

Thus in terms of σ_n^2 we can obtain the variance of the displacement error $\sigma_{y-N}^2(z)$ due the presence of noise in the experimental data:

$$\sigma_{y-N}^2(z) = \sigma_n^2D^2\mathbf{P}(z)\mathbf{\Phi}^+(\mathbf{\Phi}^+)^T\mathbf{P}(z)^T. \tag{18}$$

Using the above formula for the standard deviation $\sigma_{y-N}(z)$ we can obtain an error bound $(y(z, t) \pm \sigma_{y-N}(z))$ on the reconstructed displacement.

This method is applied to the reconstruction of experimental data from NDP tests. For a typical experimental dataset, the sensor noise level can be obtained from the rms of a segment of the signal when the riser is not being towed (zero velocity case). Fig. 15 depicts a study for a NDP dataset 2360 corresponding to a linearly sheared current profile with $U_{\max} = 0.8 \text{ m s}^{-1}$, for which the σ_n is estimated to be around 0.5%. To estimate σ_n we took the absolute value of all the CF strain measurements and then took the average along the span. Taking the absolute value prevents the noise from being cancelled off. As a result, taking the ratio of the rms of this span-averaged signal when the current velocity is zero (represents noise) and rms of the span-averaged signal when current is applied gives a measure of the sensor noise level σ_n . We also note that during the experiment, additional noise is also possible due to the experiment setup like the vibration of the carriage.

Fig. 16 depicts the rms displacement $y_{rms}(z)$ and the error bound $(y_{rms}(z) \pm \sigma_{y-N}(z))$ assuming two separate values of $\sigma_n = 0.5\%$ and 5% , for two NDP datasets 2360 ($U_{\max} = 0.8 \text{ m s}^{-1}$) and 2460 ($U_{\max} = 1.8 \text{ m s}^{-1}$). Clearly, when the assumed noise level in the experimental data is small, the variability during reconstruction is also small. As shown in Fig. 16, a larger noise level would result in a consequent increase in the level of uncertainty during reconstruction. Note that we have used data from all the working sensors (that is 8 accelerometers and 24 strain gauges for dataset 2360, and 8 accelerometers and 23 strain gauges for dataset 2460), and have used 11 sine and 14 cosine terms during the reconstruction.

7.2. Uncertainty from the use of finite number of sine and cosine terms

The reconstruction method uses a finite number of sine and cosine terms while assembling the $\mathbf{\Phi}$ matrix which may result in some error during reconstruction. We aim at quantifying this source of error during reconstruction. If the number of sine and cosine terms used in the $\mathbf{\Phi}$ matrix (limited by number of sensors available) is large, then the error is close to zero. However, error arises due to the presence of a finite number of terms which may not be able to represent the displaced shape of the riser completely. Since we do not know the adequate number of sine and cosine terms apriori, we can perform several reconstructions each utilizing a different set of sine and cosine terms. Each such set of sine and cosine terms may result in a different reconstructed riser response. If the reconstruction is sensitive to the number of sine and cosine terms used, then there is a large variability in each instance of the reconstructed riser response.

To quantify this uncertainty, we vary the number of sine and cosine terms and correspondingly obtain the resulting reconstructed displacements. Assume that each choice of the set of sine and cosine terms is represented by an index h , where $h = 1, 2, 3, \dots$, and the corresponding reconstruction using the h th set to be denoted by $y_h(z, t)$. We can use these reconstructed displacements, to obtain a measure of the variability in the reconstructions arising from the use of each set of sine and cosine terms. This variability in the reconstructed response is captured in the standard deviation $\sigma_{y-H}(z)$,

$$\sigma_{y-H}(z) = \mathbb{S}\{y_{rms_1}(z), y_{rms_2}(z), y_{rms_3}(z), \dots, y_{rms_h}(z), \dots\}, \tag{19}$$

where $y_{rms_h}(z)$ represents the rms (taken in time) of the h th reconstruction $y_h(z, t)$, and $\mathbb{S}\{ \}$ denotes the standard deviation operator. In a similar manner, the corresponding best estimate of the rms displacements can also be computed.

We apply the above method to obtain a reconstruction error bound $(y_{rms}(z) \pm \sigma_{y-H}(z))$ on NDP data. The best estimate of rms displacement $y_{rms}(z)$ (in blue color) and the error bound $(y_{rms}(z) \pm \sigma_{y-H}(z))$ due to the use of a finite number of sine and cosine terms for various NDP datasets are produced in Fig. 17. Note that we consider each of the uncertainty independently, and while considering the uncertainty due to sine and cosine terms we assume that uncertainty due to the other two factors to be zero. We also use data from all the sensors available to us. We can observe that with increase in flow velocity, the corresponding error bound increases in its magnitude. Fig. 18 illustrates

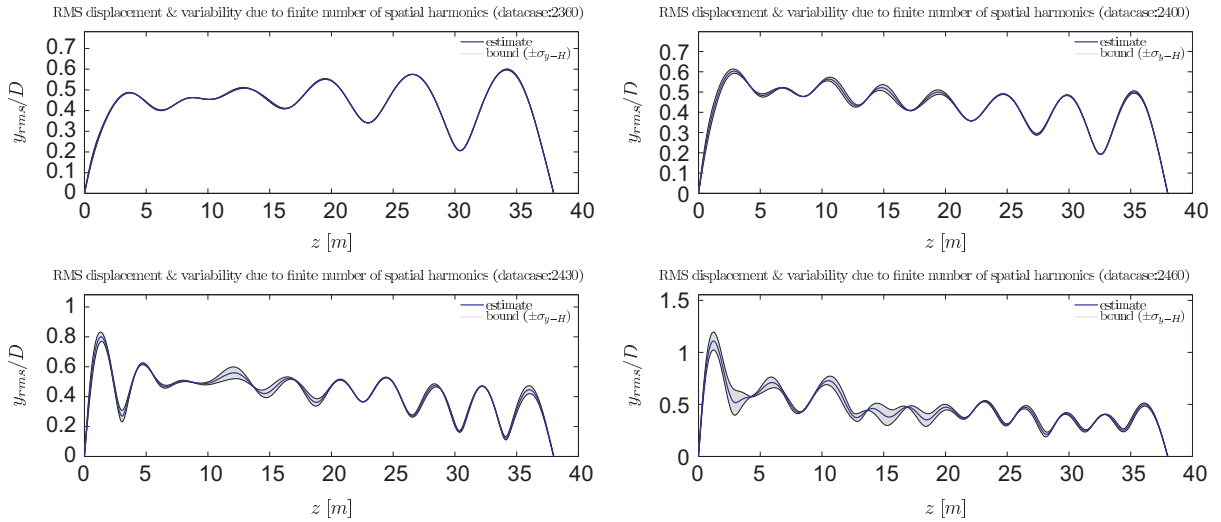


Fig. 17. Uncertainty arising due to the use of finite number of spatial harmonics during reconstruction. *Top left*: rms displacement and error bound for NDP dataset 2360 ($U_{\max} = 0.8 \text{ m s}^{-1}$); *top right*: rms displacement and error bound for NDP dataset 2400 ($U_{\max} = 1.2 \text{ m s}^{-1}$); *bottom left*: rms displacement and error bound for NDP dataset 2430 ($U_{\max} = 1.5 \text{ m s}^{-1}$); *bottom right*: rms displacement and error bound for NDP dataset 2460 ($U_{\max} = 1.8 \text{ m s}^{-1}$). Note that as the flow velocity increases, the uncertainty in reconstruction increases due to the presence of higher spatial harmonics in the measured riser motions.

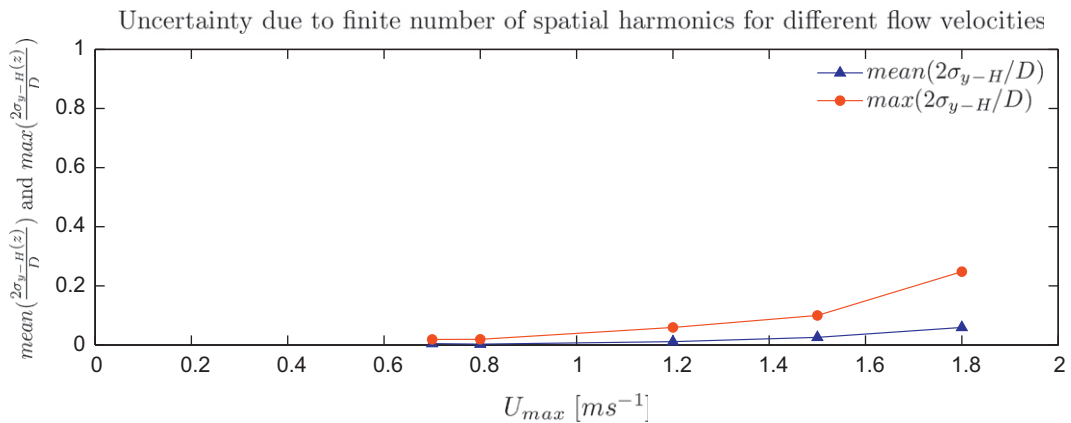


Fig. 18. Uncertainty arising due to the use of finite number of spatial harmonics during reconstruction for various linearly sheared flow velocity cases. Note that as the flow velocity increases, the uncertainty in reconstruction increases due to the presence of higher spatial harmonics in the data.

this trend, where the mean and maximum values of the reconstruction error bounds are plotted for various linearly sheared flow profiles. This happens due to the fact that with increasing flow velocity, the peak response frequencies increase and consequently the excited wave numbers increase. The limited number of sine and cosine terms (limited due to the number of sensors available) are not able to capture all the intricate details of such riser VIV motions.

7.3. Uncertainty from the presence of both acceleration and strain measurements

Depending on the length of the riser and the flow conditions, the relative magnitudes of the acceleration measurements and curvature measurements may vary. If the acceleration signals are several orders of magnitude smaller than the curvature signals, or vice-versa, then the data from those sensors may not be taken into account during reconstruction. The result is a system which may be ill-conditioned producing erroneous answers. In fact during

reconstruction, both Φ and \hat{Y} matrices consist of rows corresponding to curvatures (Φ_κ and \hat{Y}_κ) and rows corresponding to accelerations (Φ_a and \hat{Y}_a). As a result, the Φ and \hat{Y} matrices can be written as

$$\Phi \equiv \begin{bmatrix} \Phi_a \\ \Phi_\kappa \end{bmatrix} \quad \text{and} \quad \hat{Y} \equiv \begin{bmatrix} \hat{Y}_a \\ \hat{Y}_\kappa \end{bmatrix}. \tag{20}$$

The elements of Φ_κ and Φ_a are in fact the terms in front of the unknowns \hat{w} in

$$\begin{bmatrix} \Phi_a \\ \Phi_\kappa \end{bmatrix} \hat{w} = \begin{bmatrix} \hat{Y}_a \\ \hat{Y}_\kappa \end{bmatrix}. \tag{21}$$

One measure of the relative importance of Φ_κ and Φ_a are their Frobenius norms³ $\|\Phi_\kappa\|_F$ and $\|\Phi_a\|_F$. Ideally the rows corresponding to curvature could be divided by the Frobenius norm $\|\Phi_\kappa\|_F$, and the rows corresponding to acceleration could be divided by the Frobenius norm $\|\Phi_a\|_F$. We introduce a parameter β which allows for changing the relative importance of Φ_κ and Φ_a , respectively. Using β , we reassemble the system of Eq. (21) in the following form

$$\begin{bmatrix} \beta\Phi_a \\ \Phi_\kappa \end{bmatrix} \hat{w} = \begin{bmatrix} \beta\hat{Y}_a \\ \hat{Y}_\kappa \end{bmatrix}. \tag{22}$$

This section studies the uncertainty as a result of varying the relative magnitudes of the Φ_κ and Φ_a using the parameter β . For each value of the scaling factor β , we obtain an associated reconstruction. Assume that each choice of β is represented by g , where $g = 1, 2, 3, \dots$ and the corresponding reconstruction by $y_g(z, t)$. The variability in the reconstructed response is captured by the variance $\sigma_{y-\beta}^2(z)$ obtained by evaluating the various reconstructions for a range of values taken by β as

$$\sigma_{y-\beta}(z) = \mathbb{S}\{y_{\text{rms}_1}(z), y_{\text{rms}_2}(z), y_{\text{rms}_3}(z), \dots, y_{\text{rms}_g}(z), \dots\}, \tag{23}$$

where $y_{\text{rms}_g}(z)$ represents the rms (taken in time) of the g th reconstruction $y_g(z, t)$, and $\mathbb{S}\{\}$ represents the standard deviation operator. In a similar fashion, we can also compute the best estimate of the rms displacements.

We apply our methodology to datasets from NDP experiments. The Frobenius norm of $\|\Phi_\kappa\|_F$, and the Frobenius norm of $\|\Phi_a\|_F$ were found to be of similar magnitudes. Parameter β is varied from 0.1 to 10. In total, 20 different reconstructions are performed ($g = 1, 2, 3, \dots$) for each dataset corresponding to 20 different values of β . The standard deviation $\sigma_{y-\beta}(z)$ due to the variability in β is obtained, and the error bound on reconstruction is obtained as $y_{\text{rms}}(z) \pm \sigma_{y-\beta}(z)$. As in the previous uncertainty evaluations, we consider them one by one and the evaluation due to the uncertainty due to β is performed by keeping the uncertainty due to other two factors to be zero and use data from all the available number of sensors. Figure 19 depicts the best estimate of the rms of displacements and the error bounds due to the variation in β for four separate datasets from NDP experiments. As observed from Fig. 19, the variability in reconstruction increases with increasing flow velocity. For the examples in Fig. 19, we have used 11 sine and 14 cosine terms during the reconstruction.

7.4. Total uncertainty

Methods to quantify the variability arising from three sources of uncertainty in terms of their variances $\sigma_{y-N}^2(z)$, $\sigma_{y-H}^2(z)$ and $\sigma_{y-\beta}^2(z)$ are now available. However, we are interested in quantifying the total variance $\sigma_y^2(z)$ which takes into account each of the three sources of uncertainty. If we assume that the three sources of uncertainty are independent of each other, then we can obtain the total variance $\sigma_y^2(z)$ from the individual variances as

$$\sigma_y^2(z) = \sigma_{y-N}^2(z) + \sigma_{y-H}^2(z) + \sigma_{y-\beta}^2(z). \tag{24}$$

We obtain the total variance for datasets from NDP experiments. Fig. 20 depicts the estimate of the rms of the riser displacement $y_{\text{rms}}(z)$ with the variability during reconstruction ($y_{\text{rms}}(z) \pm \sigma_y(z)$) which takes into account all the three sources of uncertainty. This corresponds to an assumed noise level of 0.5%, β within the range [0.1, 10] and 8 different combinations of sine and cosine terms. We observe that as the flow velocity increases, the quality of reconstruction may decrease (variability of reconstruction increases) primarily due to an increase in the uncertainties arising from the use of a finite number of sine and cosine terms. Note that the total variance $\sigma_y^2(z)$ obtained during reconstruction is conservative in nature. This is in part due to our assumption that various sources of uncertainty are independent of each

³Frobenius norm $\|\mathbf{A}\|_F$ of a matrix \mathbf{A} is defined as: $\|\mathbf{A}\|_F = \sum_i \sum_j a_{ij}^2$.

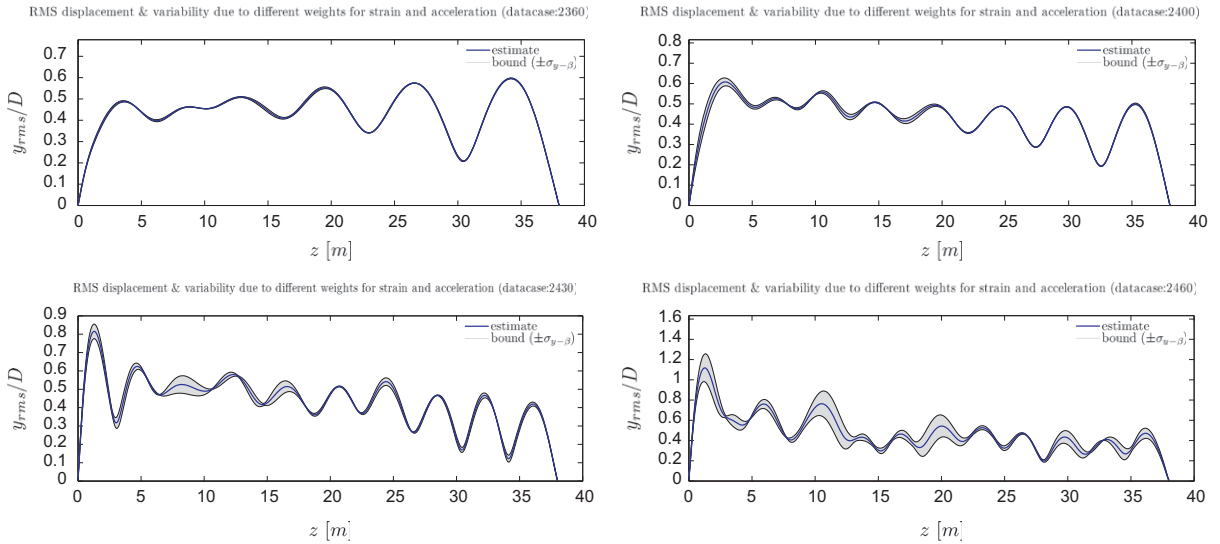


Fig. 19. Uncertainty arising due to the use of both strain and acceleration signals during reconstruction for NDP datasets 2360 with $U_{max} = 0.8 \text{ m s}^{-1}$ (top left), 2400 with $U_{max} = 1.2 \text{ m s}^{-1}$ (top right), 2430 with $U_{max} = 1.5 \text{ m s}^{-1}$ (bottom left) and 2460 with $U_{max} = 1.8 \text{ m s}^{-1}$ (bottom right). We can observe that with increase in flow velocity, the variability in reconstruction increases.

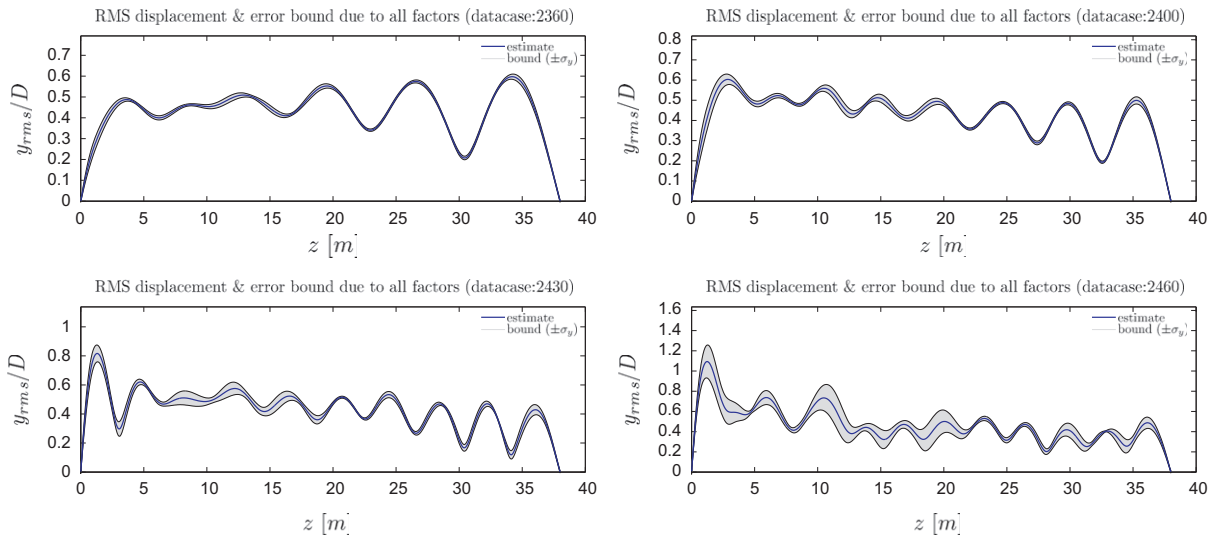


Fig. 20. Depicts the rms riser displacements and the bounds $y_{rms}(z) \pm \sigma_y(z)$, which take into account three sources of uncertainty for NDP datasets 2360 with $U_{max} = 0.8 \text{ m s}^{-1}$ (top left), 2400 with $U_{max} = 1.2 \text{ m s}^{-1}$ (top right), 2430 with $U_{max} = 1.5 \text{ m s}^{-1}$ (bottom left) and 2460 with $U_{max} = 1.8 \text{ m s}^{-1}$ (bottom right). We can observe that the total variability in reconstruction increases as the flow velocity increases.

other. The shaded regions gives us an estimate of the confidence bound on reconstruction using the method for the case of large number of sensors. Similar analysis may be performed on the confidence bound for reconstruction using the method for the case of few number of sensors. However, such an analysis will contain several more factors which will affect the uncertainty and such an extensive analysis is not within the purview of this paper.

8. Concluding remarks

What we have achieved is a systematic and scalable approach to reconstruct the VIV response of a riser using the data from a limited number of sensors (strain gauges, accelerometers) placed along the length of the riser. When the number

of sensors are large enough to capture the spatial characteristics of the riser VIV motions, the problem is posed as a spatial Fourier decomposition. This method requires no information on the riser VIV response modes and is hence independent of riser VIV predictive capabilities. The criterion for full reconstruction is evaluated from both a matrix inversion perspective and from a signal processing perspective. When we have data from a few sensors, a reconstruction method based on modal decomposition is developed. This approach employs the analytically evaluated peak response modes and peak response frequencies, and utilizes the band-separated nature of the riser VIV response. Examples using the data from NDP experiments illustrate the methods. Finally a systematic approach to quantify the various sources of uncertainty during the reconstruction is also developed.

In Section 2, we posed the problem as a Fourier decomposition without any information on the riser properties or the flow properties. On the other hand, the method described in Section 4 requires both the riser and flow properties in addition to the need for a prediction program to obtain the peak response modes and peak response frequencies. Since we have a theoretical prediction model for the vortex-induced motions only in the cross-flow direction, the reconstruction method for few sensor case in its present form is applicable only for reconstructing the cross-flow motions of the riser.

The reconstruction method for the large number of sensor case is accurate when the full reconstruction criterion is satisfied. For most NDP bare riser datasets this criterion is satisfied and allows reconstruction of the harmonic part of the riser VIV response. The reconstruction method when applied to experimental data enables us to perform several analyses resulting in improved understanding of riser VIV as described in Mukundan (2008). In this paper, we mention one of the applications on identifying the evolution and mechanism of traveling waves in riser VIV response. Reconstructed riser VIV motions clearly depict the presence of traveling waves (with consistent direction of travel in sheared current profiles and irregular direction of travel in uniform current profiles).

For reconstruction using few sensor data, it was shown that the reconstruction accuracy critically depends on our estimate of the peak response modes and peak response frequencies. Since the peak response modes and peak response frequencies depend on the flow profile, it is shown that reconstruction depends on the accuracy of obtaining the flow profile. To improve the accuracy of reconstruction we develop a method to locally correct the lift coefficient databases. The reconstruction method is applied to experimental data from NDP experiments which clearly depict the importance of using the corrected databases.

Acknowledgments

The authors gratefully acknowledge the financial support from the MIT-BP Major Projects Program, monitored by Neil Kitney and Pierre Beynet; as well as the generous permission by the Norwegian Deepwater Programme, provided through Dr. Kjetil Skaugset, to use the experimental data on a 38 m riser model.

References

- Braaten, H., Lie, H., 2004. NDP riser high mode VIV tests main report. Main report number 512394.00.01, Norwegian Marine Technology Research Institute.
- Graff, K.F., 1991. Wave Motion in Elastic Solids. Dover Publications, New York.
- Kaasen, K.E., Lie, H., Solaas, F., Vandiver, J.K., 1997. Norwegian deepwater program: analysis of vortex-induced vibrations of marine risers based on full-scale measurements. In: Proceedings of the Offshore Technology Conference (OTC).
- Lie, H., Kaasen, K.E., 2006. Modal analysis of measurements from a large-scale VIV model test of a riser in linearly sheared flow. *Journal of Fluids and Structures* 22 (4), 557–575.
- Lucor, D., Mukundan, H., Triantafyllou, M.S., 2006. Riser modal identification in CFD and full-scale experiments. *Journal of Fluids and Structures* 22 (6–7), 905–917.
- Morgan, F.D., Rao, R.V.N., 2006. Course Note for: Data and Models (12.515). Massachusetts Institute of Technology, Cambridge, MA, USA.
- Mukundan, H., 2008. Vortex-induced vibration of marine risers: motion and force reconstruction from field and experimental data. Ph.D. Thesis, Massachusetts Institute of Technology, Cambridge, MA, USA.
- Mukundan, H., Chasparis, F., Hover, F.S., Triantafyllou, M.S., 2009. Optimal VIV lift force coefficient databases from riser experiments. *Journal of Fluids and Structures* 26(1), 160–175.
- Nyquist, H., 1928. Certain topics in telegraph transmission theory. In: Proceedings of the Winter Convention of the AIEE, New York, NY, USA.
- Oppenheim, A.V., Willsky, A.S., Nawab, S.H., 1997. Signals and Systems. Prentice Hall, Upper Saddle River, NJ, USA.

- Shannon, C.E., 1949. Communication in the presence of noise. In: *Proceedings of the Institute of Radio Engineers*, vol. 37, issue 2, pp. 10–21.
- Triantafyllou, G.S., 1998. Vortex induced vibrations of long cylindrical structures. In: *Proceedings of 1998 ASME Fluids Engineering Division Summer Meeting (FEDSM98)*. Washington, DC.
- Triantafyllou, M.S., 2006. VIVA: programs for calculating riser vortex induced oscillations and fatigue life. Testing Tank Facility, Massachusetts Institute of Technology, Cambridge, MA, USA.
- Trim, A.D., Braaten, H., Lie, H., Tognarelli, M.A., 2005. Experimental investigation of vortex-induced vibration of long marine risers. *Journal of Fluids and Structures* 21, 335–361.
- Vandiver, J.K., 2003. SHEAR7 User Guide. Department of Ocean Engineering, Massachusetts Institute of Technology, Cambridge, MA, USA.
- Vandiver, J.K., Marcollo, H., 2003. High mode number VIV experiments. In: *IUTAM Symposium on Integrated Modeling of Fully Coupled Fluid-Structure Interactions Using Analysis, Computations and Experiments*. Kluwer Academic Publishers, Dordrecht.